Remote sensing and seismic data integration for the characterization of a rock slide and an artificially triggered rock fall

Marta Guinau[a],[*], Mar Tapia[a],[b], Cristina Pérez-Guillén[a], Emma Suriñach[a],[b], Pere Roig[a], Giorgi Khazaradze[a], Marta Torné[a], Manuel Jesús Royán[a], Anna Echeverria[a]

[a] Grup RISKNAT, Institut Geomodels, Universitat de Barcelona, Faculty of Earth Sciences, Department of Earth and Ocean Dynamics, Barcelona, Spain
[b] Laboratori d'Estudis Geofísics Eduard Fontserè, Institut d'Estudis Catalans (LEGEF-IEC), Barcelona, Spain

ARTICLE INFO

ABSTRACT

On May 5th, 2013 a planar rock slide ($\sim$450 m^3) occurred in the village of La Riba (NE Spain), which forced the closure of the road C-240z for 6 months. This slide left a hanging block ($\sim$130 m^3) suspended on the slope forcing a controlled blasting, followed by rock slope stabilization works. The volume of rock displaced during the both events was deduced from LiDAR and photogrammetry data following two approaches: subtracting pre- and post-event data and reconstructing the volume by fitting planes on the structural surfaces after a structural analysis of the slope. Information about the natural rock slide was obtained from the records of two permanent broadband seismic stations located 10 km from the site. From these seismic records, the existence of a rock slide was confirmed and its time of occurrence was determined, information that would be otherwise unknown. In addition, despite the small volume displaced during the event, its location was deduced from a single seismic station analysis. The blasting process was recorded with two high-definition (HD) video cameras and by two temporary seismic stations deployed close to the site ($<$ 100 m). Both the seismic and video recordings enabled us to reconstruct the trajectories and propagation details of the blasted rock blocks, involving material of different size sliding on the slope, suspended in the air or bouncing and impacting along the slope and on the road. Potential and seismic energy ratios (E_s/E_p) for each event were calculated from seismic data analysis in order to investigate the possibility of estimating properties of the rockfalls, primarily volume. The potential energy of both events was deduced from the volumes calculated using remote sensing methods and ranged between 189 and 201 MJ for the natural rock slide and between 48 and 54 MJ for the artificially triggered rockfall. The seismic energy was calculated following two approaches; estimating pseudo local magnitudes and by classical wave propagation theory, obtaining E_s values ranging from 2.0×10^{-1} MJ to 4.4×10^{-1} MJ for the natural rock slide and from 4.5×10^{-3} to 9.1×10^{-3} MJ for the artificial event. We estimated ranges of E_s/E_p ratios between 1.5×10^{-7} and 5×10^{-3} for the natural rock slide and between 8.5×10^{-5} and 1.1×10^{-4} for the artificial rockfall. The comparison of the volumes calculated using these ratios with the realistic volumes estimated from remote sensing data analysis, show that the seismic method is far less reliable for this task, specifically for small volumes ($<$ 500 m^3) at long distances ($>$ 10 km). Partially, because only a part of the released energy is transmitted into the ground as seismic energy, and partially because the recorded seismic signal is highly dependent on the event characteristics and the geotechnical conditions of the ground materials. Nevertheless, seismic data is very well suited to detect and characterize in detail both rockfall events of different nature and size. Merging and integrating remote sensing techniques such as LiDAR or photogrammetry with seismic measurements should allow the implementation of rockfall early warning systems.

1. Introduction

During the last few decades, 3D data acquisition by remote sensing techniques such as laser scanning or photogrammetry, together with the development of innovative data processing methods, have provided new opportunities for the detection, characterization, and monitoring of rock slope instabilities (Abellán et al., 2014, 2016; Jaboyedoff et al., 2012). These techniques provide data after (and sometimes before) the

---

event, allowing the analysis of the volume of detached material, the structural characteristics of the affected area, and the detection of precursory indicators of a larger event (Deparis et al., 2008a; Mavrouli and Corominas, 2017; Royán et al., 2014; Tannant et al., 2017). Moreover, 4D monitoring routines have been developed with LiDAR and photogrammetry data to analyze magnitude-frequency relationships with quasi real-time monitoring (Williams et al., 2018). However, the relatively low temporal resolution associated with scarce measurements, hinders obtaining more detailed insights on the individual stages of the single event (i.e., detachment, fall, impact, and disintegration) (Dietze et al., 2017).

In recent years, among all the contemporary methods commonly used for rockfall monitoring, seismic methods have been gaining popularity due to their potential of detecting remotely the occurrence and the location of these events (Deparis et al., 2008b; Vilajosana et al., 2008; Bottelin et al., 2014; Lacroix and Helmstetter, 2011; Hibert et al., 2014; Tripolitsiotis et al., 2015). More commonly, this was done using permanent seismic networks (e.g., Deparis et al., 2007; Moore et al., 2017), enabling the detection of large events (with volumes exceeding $1000\,\mathrm{m}^3$) at distances of up to hundreds of kilometres (Dammeier et al., 2011). However, during the last decade, local seismic networks have also been specifically installed to monitor rockfalls (e.g., Spillmann et al., 2007; Lacroix and Helmstetter, 2011; Moore et al., 2011), which enable the detection of smaller events. In general, these seismic data of rockfall events are very valuable, as they often constitute the only information available to characterize and localize events. Most authors conclude that a network of seismic sensors is required to accurately localize a specific event, using for example beam-forming (Lacroix and Helmstetter, 2011; Bottelin et al., 2014), the amplitude source location (Battaglia and Aki, 2003) and the signal migration (Burtin et al., 2014; Dietze et al., 2017) methods. Alternative methods are based on the arrival times of typical seismic phases, requiring only a few stations to localize earthquakes. For example, using single station method (Alessandrini et al., 1994; Havskov et al., 2012), it's possible to estimate the location of a seismic source using only one seismic sensor but with less accuracy.

Apart from localization, seismic signals can be used to estimate the volume of the fallen material (Dammeier et al., 2011; Deparis et al., 2008b; Hibert et al., 2011; Yamada et al., 2012). Hibert et al. (2011) estimated the volumes of hundreds of rockfalls using seismic signals based on the ratio of seismic to potential energy. The ratio calculated by various authors range from low 10^{-7} (Weichert et al., 1994), to medium 10^{-4} (Hibert et al., 2011; Bottelin et al., 2014), and high, 0.25 conversion ratios (Vilajosana et al., 2008). As pointed out by Suriñach et al. (2018), the methods for seismic energy computation are greatly dependent on the laws of attenuation with distance, demanding the knowledge of generally unknown ground parameters and possible local site effects. Therefore, it is very difficult to find consistent estimates of the released energy due to high variability in i) the nature of the rockfall events, ii) the source-receiver distances, and iii) the geotechnical ground conditions. Among the studies that analyze rockfalls from seismic signals one can distinguish studies that: a) use seismic signals induced by large volume events ($> 1000\,\mathrm{m}^3$) recorded by permanent seismic stations usually located at long distances ($> 10\,\mathrm{km}$) (Deparis et al., 2007; Moore et al., 2017); and b) characterize small volume events ($< 1000\,\mathrm{m}^3$) from the seismic signals recorded at temporary seismic sensors at short distances ($< 10\,\mathrm{km}$) (Hibert et al., 2017; Saló et al., 2018; Vilajosana et al., 2008).

Recent studies have demonstrated that high frequency seismic signals provide additional information regarding the source mechanism and failure dynamics of rock cliffs and slopes (Hibert et al., 2017; Saló et al., 2018; Zimmer and Sitar, 2015). High frequency seismic signals, however, are attenuated much faster with distance than low frequency ones due to intrinsic attenuation and wave scattering in the small-scale heterogeneities of the terrain. Hence, the recorded frequency content is highly dependent on the source-receiver distances.

Farin et al. (2015) and Dietze et al. (2017) point out that very few rockfall areas are analyzed using a combination of the seismic and optical or remote sensing techniques. Hence, it is difficult to confirm event characteristics from seismic data with other independent information. Several studies have shown that rockfall dynamics can be characterized using the combination of seismic signals with remote sensing or video recordings (Bottelin et al., 2014; Dammeier et al., 2011; Hibert et al., 2017; Vilajosana et al., 2008). So far, the combination of remote sensing techniques such as LiDAR and photogrammetry with seismic measurements is still scarce (e.g., Bottelin et al., 2014; Dietze et al., 2017) and hence, additional calibration works are needed, as it is done in this study, to corroborate the usefulness of combining the both methods.

In this study, we combine seismic and remote sensing techniques to: 1) demonstrate how the location of a rockfall event can be deduced by means of only one permanent seismic station, even when the displaced volume is small ($< 1000\,\mathrm{m}^3$) and/or the distance is large ($> 10\,\mathrm{km}$); 2) investigate the possibility of estimating physical properties of the rockfalls, primarily volume, solely based on the analysis of the seismic data; and 3) explore whether the characteristics of an event can be deduced in the same way for small events ($< 1000\,\mathrm{m}^3$) recorded at nearby temporal seismic stations and for large events ($> 1000\,\mathrm{m}^3$) recorded at permanent stations located at greater distances ($> 10\,\mathrm{km}$).

The term "rockfall" (one word) is used in this paper as a general term describing all events with a rock mass detaching and propagating on a steep slope, regardless of volume, dynamics or failure mode. When a specific rockfall type will be discussed the term "rock slide" will be used for rock blocks sliding on a planar inclined surface, and the term "rock fall" (two words) will be used for a rock detachment event involving rock blocks falling, rolling or bouncing down the slope, following Hungr et al. (2014).

The paper starts by describing in Section 2 the natural rock slide that occurred in spring of 2013 on a rock slope located near the village La Riba (NE Iberian Peninsula), as well as the rock fall triggered by the subsequent blasting carried out to remove the remaining unstable blocks (Fig. 1). In Section 3, we introduce the technical characteristics of the remote sensing methods used in this paper (LiDAR and photogrammetry) and the seismic sensors. The rock slope structure characterization in Section 4 and volume estimation in Section 5 were performed using terrestrial and aerial LiDAR data and photos acquired both before and after the natural rock slide and the subsequent blasting. In Section 6, the detection and location of the natural rock slide is described. The chronology of the successive rock fall phases during the artificially induced event was characterized in Section 7 from the seismic data and two HD video recordings. In Section 8 we estimate the seismic energy and the ratios of seismic to potential energy of the natural (Section 8.1) and the artificially induced (Section 8.2) events. Finally, a discussion on the main results and conclusions are presented in Section 9. Supplementary data deduced from the seismic signals are provided in the Data in Brief article (Tapia et al., submitted).

2. Study area and events description

A natural rock slide (hereinafter NR) occurred on May 5th, 2013 in La Riba (Tarragona, Spain), at 347983 E, 4575793 N (UTM ETRS89-Zone 31 N) (Fig. 1). The affected rock slope is composed of Upper Muschelkalk limestones. The dominant discontinuity set corresponds to the stratification, dipping north-eastward towards the road. The rock mass of about 8 m long, 16 m wide and 3.5 m high, slid along 15–20 m over a bedding plane, with a mean slope of 55°, before the impact onto the road pavement and the riverbed. The impact produced damage on the road and the debris deposit interrupted the traffic between the two nearby towns during a period of six months.

A rock mass of about 11 m long, 6 m wide, and 3 m high laying on top of the slip surface remained marginally stable after the natural rock slide (Fig. 1b). Part of this rock compartment was detached by two
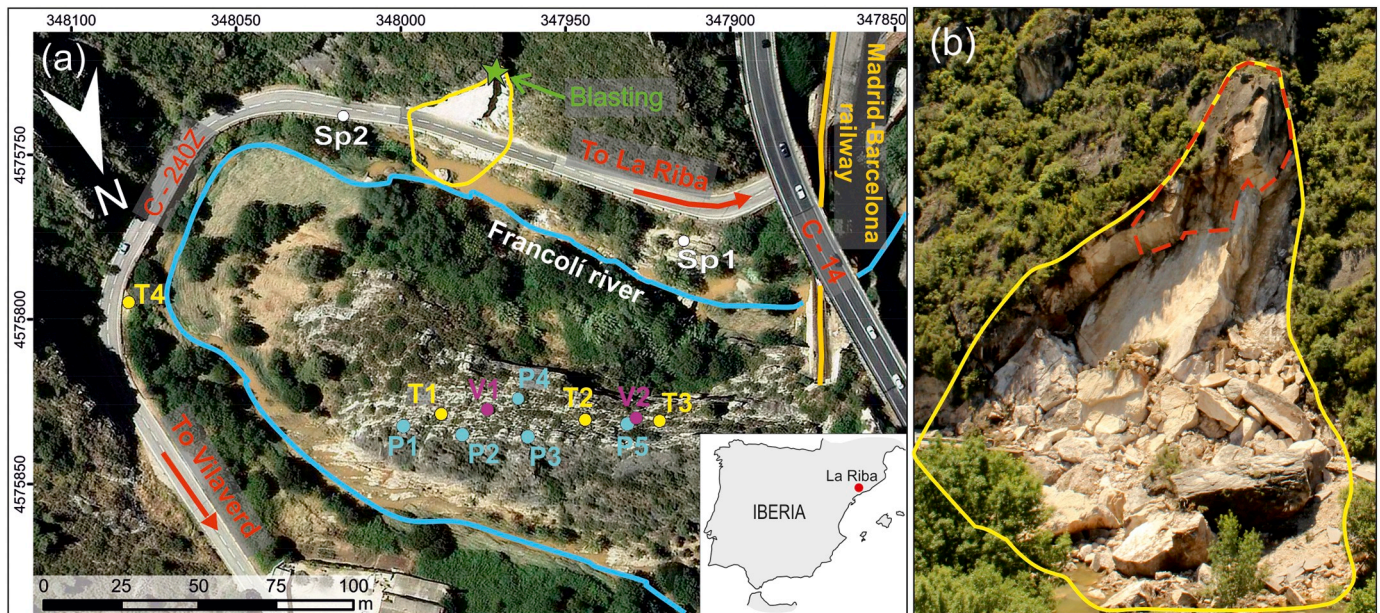
Fig. 1. General setting of the study area. (a) Orthophoto of the site with terrestrial LiDAR (TLS) data acquisition positions (T, in yellow), the camera positions (P, in light blue), the seismic stations (Sp in white), and the HD video camcorder positions (V, in purple). The yellow line delineates the area affected by the natural rock slide (NR) showed in Fig. 1b. Blast location is indicated by a green star. The Institut Cartogràfic i Geològic de Catalunya (Catalan Cartographic and Geologic service-ICGC), provided the 25 cm resolution orthophoto (Coord. Syst. UTM-ETRS89; Zone 31 N); (b) Photo of the Natural Rock slide (NR) (delineated with a yellow line) with the artificially removed (AR) rock compartments delineated with a red dashed line (photo taken from point P5 in Fig. 1a). (For interpretation of the references to colour in this figure legend, the reader is referred to the web version of this article.)

preliminary micro-blast tests (hereinafter Bt1 and Bt2) carried out on June 22nd, 2013 and August 6th, 2013 to verify that the explosions would not affect the nearby communication routes, such as the C-14 regional road and the Madrid-Barcelona railway (Fig. 1a). Afterwards, most of the rock mass was blasted on September 15th, 2013 (hereinafter Main-Blast, MB), and the rock slope was reinforced later. All these artificially triggered events are cited hereinafter as Artificial Rock falls-AR.

3. Data acquisition systems and processing

Two LiDAR data series were acquired before and after the artificially triggered rock falls (AR) (Figs. 1 and 2) with an Ilris 3D (Optech) terrestrial laser scanner. Its location was determined to a cm level accuracy using a dual-frequency GPS receiver Topcon GB-1000 with a PG-A1 antenna employing a state-of-the-art post-processing software GAMIT/GLOBK developed at MIT (Herring et al., 2015). Noisy points (mostly vegetation and points located outside the study area) were manually filtered using the PolyWorks® v10.0 - IMInspect software (InnovMetrics®), resulting in 2 point clouds, each with an average density of 332 points/m^2.

Moreover, two sets of photos (pre- and post-AR) were taken from 5 different positions (Figs. 1 and 2) using a Canon EOS-600D DSLR camera (18 megapixel resolution) with an 18–55 mm lens, shooting at 55 mm. The camera positions were obtained using same Topcon GPS system and post-processing, following the same procedure as for the LiDAR. Photos were taken with an aperture of f/22, a shutter speed of 1/80s at ISO 400. These photos (5 photos pre- and 5 photos post-AR; one photo per camera position, P in Fig. 1a) were treated with Photoscan© software (AgiSoft, 2012), obtaining two 3D point clouds with an average density of 184 points/m^2. The photogrammetric model accuracy is mostly controlled by the accuracy of the georeferencing procedure (approximately 0.02 m) and the number of photos (5 photos per model) resulting in an accuracy of 0.2 m.

In the case of the NR for the pre-sliding stage, only data from aerial LiDAR were available. These data belong to the LiDARCat project that

covers Catalonia (NE Spain) (ICGC-LiDAR data, 2017). Data acquisition was carried out between 2009 and 2011 by the Institut Cartogràfic i Geològic de Catalunya (ICGC), with a Cessna Caravan 208B aircraft equipped with a Leica ALS50-II topographic LiDAR sensor. The minimum pulse density per strip was 0.5 points/m^2 and the vertical accuracy of the LiDAR system was about 15 cm root mean square error (RMSE). The points were classified using the TerraScan© software (Terrasolid©) and a manual expert verification to identify the points corresponding to the terrain (ICGC-LiDAR data, 2017).

Two permanent broadband seismic stations recorded the NR event on May 5th, 2013. These stations are EPOB located at 9.5 km distance NW of La Riba site, belonging to the Spanish seismic network (Instituto Geográfico Nacional, IGN) and POBL located at 10.7 km NW of it, belonging to Laboratori d'Estudis Geofísics Eduard Fontserè, Institut d'Estudis Catalans (LEGEF-IEC) and the Catalan Seismic Network (ICGC-IEC, Institut Cartogràfic i Geològic de Catalunya-Institut d'Estudis Catalans, 1996) (Fig. 6c). Both stations are deployed mainly for earthquake monitoring and location in their respective regions. The EPOB and POBL stations continuously record seismic data at a sampling rate of 100 Hz and 50 Hz, respectively. They are 3-component broadband seismometers (Guralp CMG3T and Geotech KS2000M) with a flat response between 0.01 and 50 Hz (EPOB) and 0.01–25 Hz (POBL) and use 3 channel 24-bit digitizers. POBL data are available through the International Federation of Digital Seismograph Networks (FDSN, http://www.fdsn.org) and EPOB data are available on request to IGN.

Two temporary short-period seismic stations (Sp1 and Sp2 in Fig. 1a) were installed the day of the MB event to record the seismic signals generated by this event. Sp1 was set on a hard rock at 75 m from the blast site and Sp2 was set on the road pavement at 90 m from the blast site, as close as it was allowed by the authorities. These seismic stations are composed of a SpiderNano digitizer (Worldsensing©), a short period (2 Hz) 3-component seismic sensor (Miniseismonitor, Geospace Technologies®), GPS antenna for UTC time and batteries. Continuous data acquisition was performed with a 250 sps, resulting in a range of recorded frequencies of 2–125 Hz.

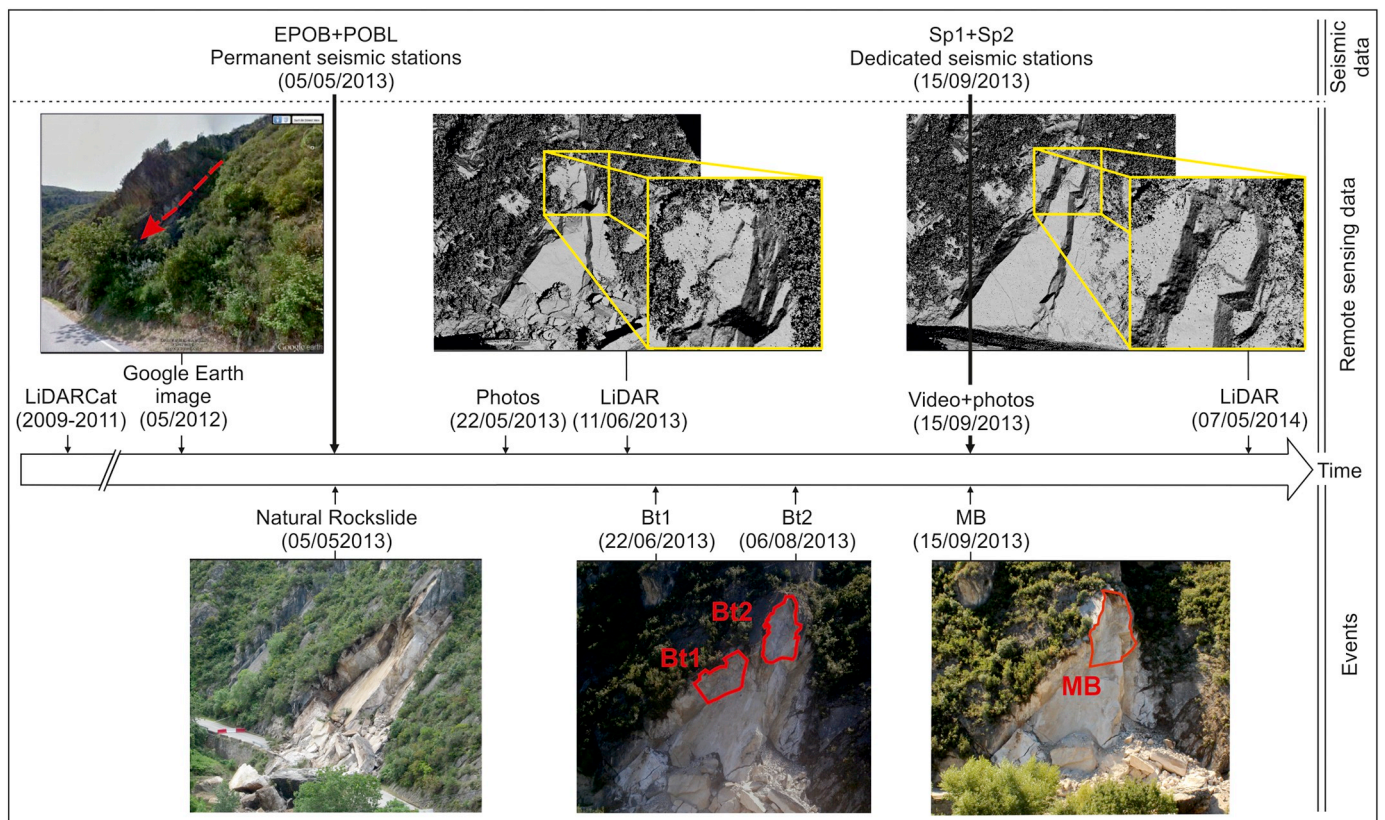In addition, two videos were recorded with two high definition

Fig. 2. Chronology of events and data acquisition. Central white arrow represents the time axis for the temporal evolution of various data acquisition surveys (top) and events (bottom). Insets on pre- and post-AR LiDAR images show an enlarged image of the blasted area, delineated with the yellow squares. The red polygons delineate the detached rock mass during the micro-blast tests (Bt1 and Bt2) and the Main-Blast (MB). (For interpretation of the references to colour in this figure legend, the reader is referred to the web version of this article.)

SONY HDV 1/3" 3CCD camcorders located at two distinct sites (Figs. 1 and 2), resulting in 1080p resolution videos with 25 frames per second.

4. Joint identification and characterization

We analyzed the slope structure and the surfaces formed as a consequence of the natural rock slide (NR) and the artificial rock falls (AR). The LiDAR and photogrammetric point clouds were treated with the SEFL (Surface Extraction From LiDAR) software (García-Sellés et al., 2011). Results are shown in Fig. 3. They are in agreement with field data (61 compass measurements in the lowest accessible part of the slope).

The main joint set F1 (Fig. 3) corresponding to the bedding and acting as the sliding surface, had a mean dip/dip direction of 55°/040°. Three additional joint sets F2, F3 and F4 were detected with mean dip/dip directions of about 70°/165°, 85°/306°, and 52°/180° respectively. Another joint set F5 (50°/310°) was detected only by field measurements since it was only observed as lineaments on the rock slope. The post-AR 3D point clouds showed a concentration of points with a dip/dip direction of 60°/210° (6 in Fig. 3c). As this orientation was not detected in pre-AR point clouds (neither with LiDAR nor with photogrammetry or, field measurements) it probably corresponds to a surface generated by the blasts.

The block compartments removed by the blasts were delimited in their upper and lower parts by surfaces from the F1 joint set. Laterally they were delimited mainly by the discontinuities corresponding to the F3 and F4 joint sets (Fig. 3). As explained in the next section, this structural analysis of the block compartments provides useful information for estimating the volume of the detached blocks, even when no pre-event data are available.

5. Volume estimation

Since the LiDAR and photogrammetry data encompass both the second Blast-test (Bt2) and the Main-Blast (MB), the volume estimation of individual events is not possible. The same restriction is often true for naturally triggered events where no pre-failure data is available. To deal with this constrain, we propose to estimate the volume of removed material following two methods: a) the subtracting volume approach, consisting in subtracting the data before and after the event, and b) the volume reconstruction approach, which consists of confining the rock compartments involved in each event by fitting planes on the controlling joints.

5.1. Subtracting volume approach

In the case of the natural rock slide (NR), we estimated its volume by subtracting the aerial LiDAR pre-failure data from the terrestrial LiDAR post-failure data. Given the different spatial resolution of aerial (pre-sliding, 0.5 points/m^2) and terrestrial (post-sliding, 332 points/m^2) point clouds, they were resampled applying a 0.5×0.5 m grid using Matlab® software (MathWorks®). We then aligned the pre- and post-failure data following two steps: a) the preliminary identification of homologous points between the point clouds, and b) the minimization of the distance between pre- and post-failure data by means of an iterative procedure using the *Iterative Closest Points* (ICP) algorithm (Chen and Mendioni, 1992), excluding failure areas. Both the first and second steps are performed in PolyWorks® v.10.0 (InnovMetrics®) using the *N-points pairs* and *Best-fit alignment* tools. Then, the distances between pre- and post-failure points were computed using the *Multiscale Model to Model Cloud Comparison* (M3C2) algorithm (Lague et al., 2013) in CloudCompare (Girardeau-Montaut et al., 2005). Finally, the volume of the natural rock slide was calculated following these four steps: a) construction of a triangulated mesh from the pre-failure points; b)
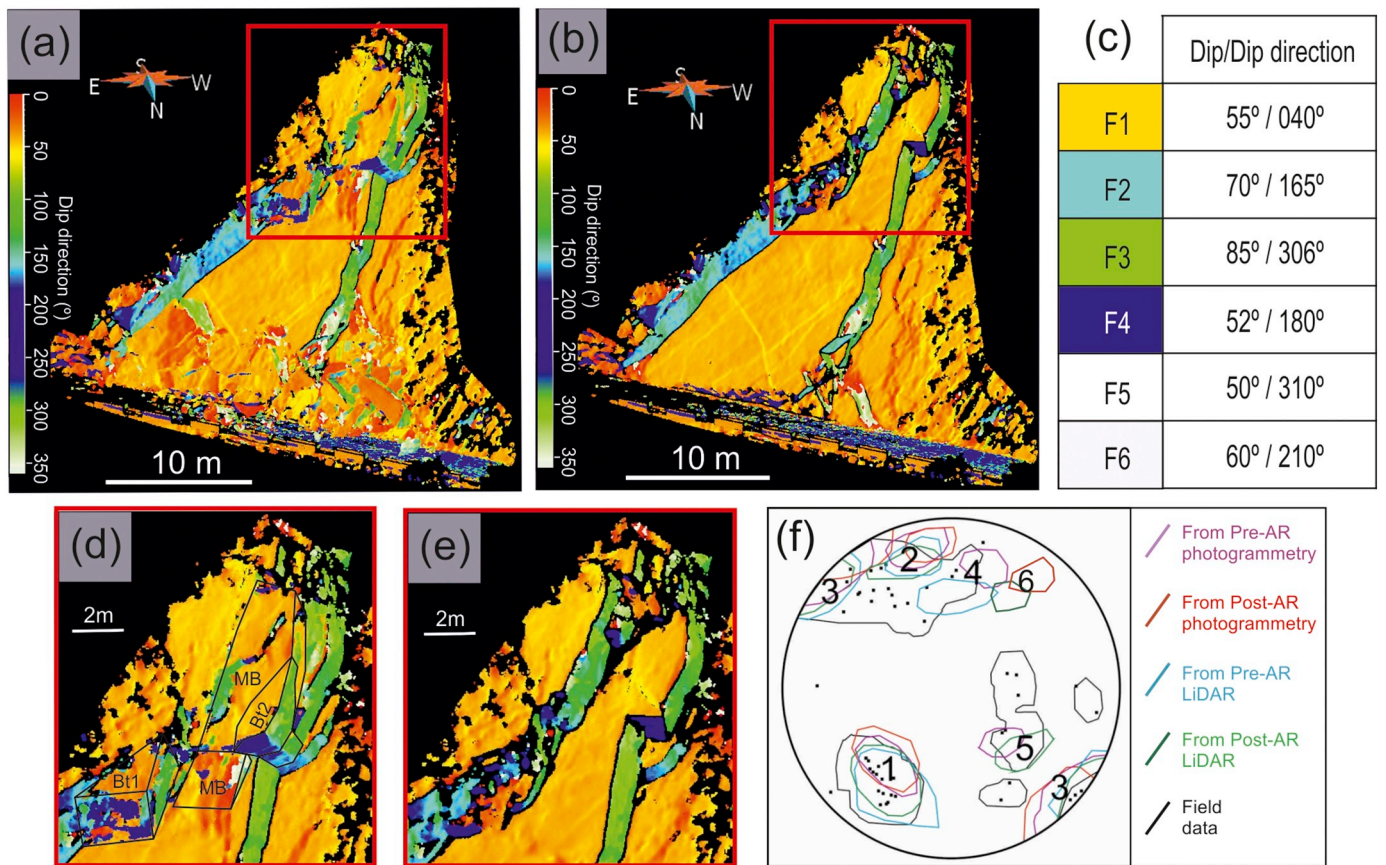
Fig. 3. Structural analysis of the study site. (a) and (b) Pre-AR and Post-AR LiDAR point clouds respectively, coloured according to the dip direction of the surfaces defining joint sets (red squares delimit the source area of the AR enlarged in (d) and (e)); (c) Table with the mean orientation of the joint sets (F1, F2, F3 and F4 are identified with the same colour as in (a), (b), (d), and (e) point clouds); (d) Enlargement of the pre-AR point cloud including the block compartments consequently removed by Bt1, Bt2, and MB (delimited by black lines); (e) Enlargement of the post-AR point cloud without the block compartments removed by the blasts. (f) Density diagram in equal area stereographic projection of discontinuity poles obtained from LiDAR (blue lines (pre-AR) and green lines (post-AR)), photogrammetry (purple lines (pre-AR) and red lines (post-AR), and field data (black dots and black lines). Scales in (a), (b), (d), and (e) are approximated because they are images of the 3D models. (For interpretation of the references to colour in this figure legend, the reader is referred to the web version of this article.)

Table 1
Volume estimations and comparison. The upper half of the table shows the volume estimations, in the left column by the subtracting volume approach and in the right column by the volume reconstruction approach. The lower half of the table shows the percentage difference between the volumes estimated from LiDAR or photogrammetry data (left column) and by using the Subtracting volume or the Reconstructing volume approach (right column).

	Volume estimation			
	Subtracting volume approach		Volume reconstruction approach	
	Photogrammetry (m^3)	LiDAR (m^3)	Photogrammetry (m^3)	LiDAR (m^3)
NR (2013/05/05)	–	475.0		506.0
Bt2 + MB	183.1	206.7	196.0	220.7
Bt2 (2013/08/06)	–	–	75.2	85.3
MB (2013/09/05)	–	–	120.8	135.4
	Volume comparison			
	Photogrammetry vs LiDAR		Subtraction vs Reconstruction	
	Subtraction (%)	Reconstruction (%)	Photogrammetry (%)	LiDAR (%)
NR (2013/05/05)	–			6.1
Bt2 + MB	11.4	11.2	6.6	6.3
Bt2 (2013/08/06)		11.8		
MB (2013/09/05)	–	10.8	–	–

computation of the area (A_i) of each triangle; c) a height (H_i) was assigned to each of the triangles taking into account the difference with the post-failure data obtained for each of the vertices of the triangle; and d) the values corresponding to the volume of each triangle ($A_i \times H_i$) are added to obtain the total volume. The final computed volume of the natural rock slide was 475.0 m^3 (Table 1).
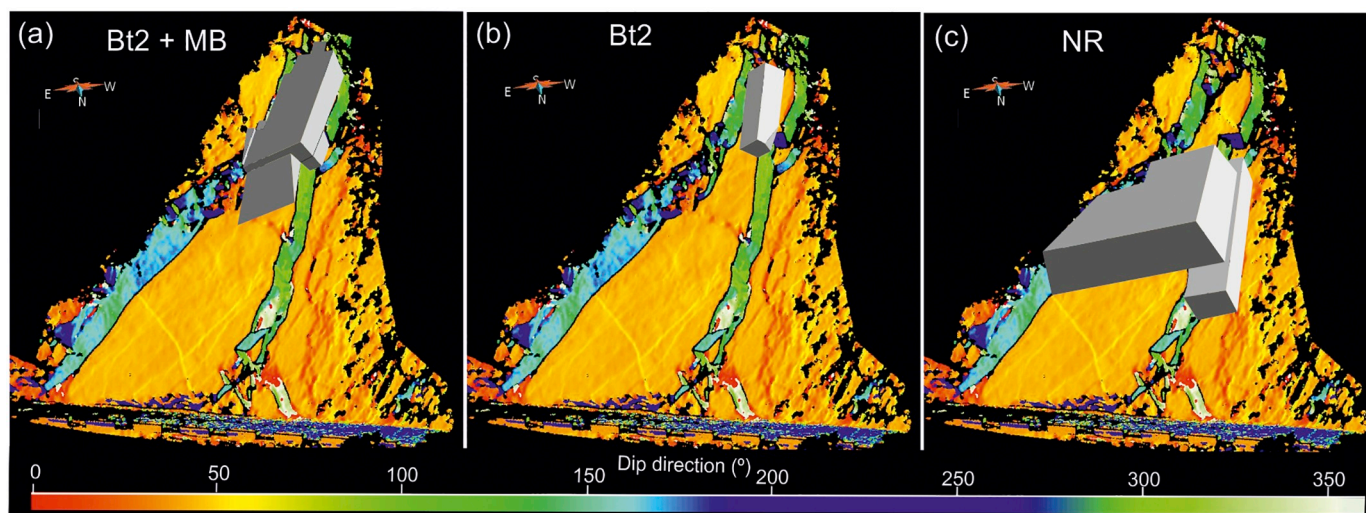
Fig. 4. Post-AR LiDAR point cloud coloured according to the dip direction of the slope with the block compartments created in Gocad® for the volume estimation following the volume reconstruction approach. The colorbar depicts the dip direction of the 3D point clouds. (a) Corresponding to Bt2 + MB; (b) Corresponding to the Bt2; and (c) Corresponding to the NR.

The volume estimation only for the main-blast (MB) was not possible due to the lack of data preceding the event. Hence, following the same steps as for the NR, the volume was obtained by subtracting pre- and post-AR data, which corresponds to the spatially coincident Bt2 and MB events (Figs. 2 and 3). The removed volumes for these events together were estimated to be 206.7 m³ and 183.1 m³ from LiDAR and photogrammetry data respectively, with a difference of 11.4% (Table 1).

5.2. Volume reconstruction approach

The difficulty of obtaining the volume of the removed material during the MB leads us to estimate the removed volume by reconstructing the rock compartments detached by Bt2 and the MB delimited by joints (Figs. 3d, 4a and b). This was performed following four steps: a) the points corresponding to each joint set were grouped into clusters so that each cluster corresponds to a different surface, performed with the SEFL software; b) with the software Gocad® (Paradigm®) a 3D surface is created from each cluster that delimits the rock compartments; c) the surfaces were enlarged to intersect them and close the volume of the blocks removed by the blasts; and d) the volume of each enclosed compartment was calculated using the tool Get Layer Volume from the Model3D menu of the Gocad® software. In order to obtain the volume only for the MB, the volume of the Bt2 compartment was subtracted from the corresponding volume to the Bt2 and MB compartments together (Table 1). The volumes obtained from LiDAR and photogrammetry data and the differences between them are summarized in Table 1.

The volume of the NR was also reconstructed using the information obtained from the structural analysis (Section 4) and the interpretation of pre-failure images. Given the lack of high-resolution images or data from the pre-failure stage, aerial photos and historic Google Earth images were used in order to reconstruct the pre-failure surfaces. The volume for the rock compartment was estimated to be 506.0 m³, with 6.12% of difference from the volume obtained with the subtracting volume approach (Table 1).

6. Analysis of the natural rock slide (NR) from seismic records: detection, characteristics and location

6.1. Natural rock slide (NR) seismic data

The two permanent seismic stations, located ~10 km from La Riba,

represent the only instrumentation present and able to register the Natural Rock slide (NR) event occurred on May 5th, 2013. The technical characteristics of these two seismic stations are described in Section 3. Although the two stations are separated only by 3 km, they are located in considerably different local geologic conditions: POBL is set on soft sediments (Pleistocene alluvial fan deposits) within the cloister of the Poblet monastery, while EPOB is set inside a cave on harder basement rocks (Carboniferous shales with sandstone intercalations).

The three components of the seismic data recorded at EPOB and POBL stations are shown in Fig. 5. The signals recorded at POBL show greater amplitudes than EPOB, mainly due to the local site effects (e.g., Bard and Bouchon, 1985; Bard and Riepl-Thomas, 2000; Thompson et al., 2009; Maufroy et al., 2016). The presence of soft sediments at POBL cause the amplification of the seismic amplitudes (see Section 2.1 in Tapia et al., submitted). In addition, the seismic signal prior to the NR event at EPOB has a background noise of $\pm$ 0.15 × 10^{-7} m/s and at POBL $\pm$ 0.30 × 10^{-7} m/s, twice as much as at EPOB. The high background noise observed at POBL is due to its location within a populated area and near a road (Fig. 6), which generates negative effects on the signal-to-noise ratio (SNR). Therefore, the geological location of EPOB and its isolation from anthropogenic noise, together with the fact that POBL has a lower frequency range (0.01–25 Hz) with respect to EPOB (0.01–50 Hz), makes EPOB preferable to study detailed characteristics of the recorded waves caused by the rockfalls at La Riba. Due to the reduced rock volume of the NR event and the relatively large distance to the seismic stations, the identification of the seismic signal induced by the NR in the continuous recording of a single station is not trivial. Thus, the POBL data was essential for a qualitative interpretation and a correct identification of the NR event and for determining its release time (08:41:40.9 UTC; Fig. 5).

Traditional seismic phase picking procedures were used to identify the first weak P-wave (P_g direct crustal arrival) from the EPOB waveform arrival, which was better observed in the EW component (08:41:40.90 UTC) (red dashed line in Fig. 5). For the POBL waveform (Fig. 5b), the P-waves are not easily appreciated because of the higher background noise. After about 2.38 s (08:41:43.28 UTC), S-waves appear as S_g direct crustal arrival (blue dashed line in Fig. 5). After 0.7 s (08:41:43.96 UTC) following the S-wave arrival, the first surface waves appear, specifically the Love waves, highlighted in the EW component at 08:41:44.88 UTC (green dashed line in Fig. 5). They are followed by more prominent Rayleigh surface waves, visible in the Z and NS
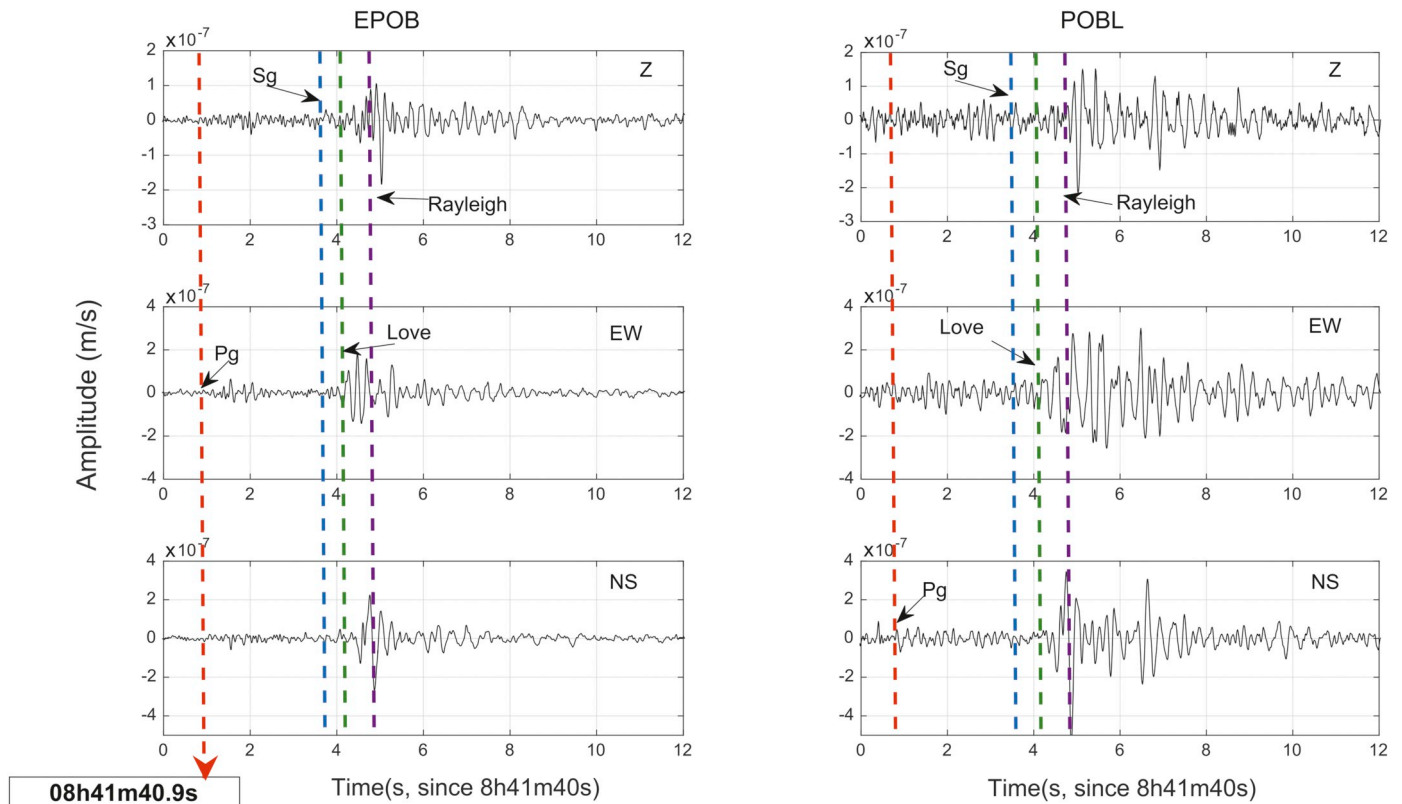
Fig. 5. Tree-component seismic records for the NR event from EPOB (left column) and POBL (right column) stations. Vertical (Z), East-west (EW) and North-South (NS). All seismic signals are filtered between 1 Hz and 25 Hz. Different waves are indicated (P_g, S_g direct crustal arrivals, Love and Rayleigh surface waves).

components (purple dashed line in Fig. 5). The identification of these waves was confirmed by a polarization particle motion analysis of all these phases (Section 2.3 in Tapia et al., submitted). According to these observations, the waveforms induced by the NR event show a pattern (P, S and superficial waves above the background noise) that suggest the occurrence of a large single impact. The recorded seismic signal could correspond to the impact of the largest slipped rock-block on the road, which is consistent with the supposed failure of the block as a whole. Other hypothetical released rock-blocks of smaller volume are unlikely to generate enough seismic energy detectable at this large source-receiver distance (around 10 km), making them indistinguishable from background noise (Fig. 5).

6.2. Natural rock slide event location

To locate the event using the single station method, the azimuth was calculated through several polarization analysis and the distance was estimated using wave identification and travel time techniques. To determine the consistency of the estimated location based on seismic data, the results are compared with the known location of the NR.

Using the three components seismic records, a polarization analysis according to Jurkevics (1988) and Vidale (1986) was carried out, following the steps described in Vilajosana et al. (2008). Our main focus was on two parameters: a) linearity (L) and b) back azimuth (θ). L is 1 in case of a perfectly linear polarized waves, and it reduces towards zero for more elliptically polarized waves. In the case of P waves, L is expected to be close to 1. The back azimuth (θ) gives the polarization direction of the incoming P waves.

The polarization analysis was applied for the first 1.3 s of the first P_g wave (Fig. 6a). As can be seen from corresponding spectrograms (Fig. 7 in Tapia et al., submitted). The main energy has been registered in the time section. The initial seismogram was filtered between 1 and 12 Hz using fourth order Butterworth filter, eliminating the high frequency

wave contribution due to scattering of the waves caused by the presence of small-scale heterogeneities in the sub-surface. The found linearity is L = 0.97, which indicates a highly linear polarized wave, confirming that the P_g waves were most likely identified correctly, and thus can provide coherent information on the true ray-path, which can be successfully used for the event location (Alessandrini et al., 1994; Havskov et al., 2012). The dominant polarization direction θ is 116.6°, which is identified as red line marked *Vidale* in Fig. 6b, together with the particle motion plot for the horizontal components of the selected wave packet.

Additionally, to confirm the previous result, a test was conducted following Alessandrini et al. (1994) and Havskov et al. (2012) methodology. The back azimuth was computed through θ = arctan(A_{EW}/A_{NS}), using the first P arrival (blue line marked Alessandrini in Fig. 6b) and measuring its EW (A_{EW}) and NS (A_{NS}) amplitudes (see amplitude values in Fig. 6a). The sign of the Z amplitude was used to solve the 180° ambiguity of the trigonometric function. The result is 116.4°, similar as the previously obtained back azimuth. Apart from the two previous computations, a linear regression for the horizontal components EW and NS was also adjusted to determine the azimuth (Linear Fitting in Fig. 6b). The result is 111.8° with a low correlation of 0.35. The orientation is concordant with the other results and with real geographical settings, where the real back azimuth estimated from EPOB to the NR site is 112.8° (Fig. 6c). In any case, the three employed methods for back azimuth calculation are in good agreement with each other. Using the obtained back azimuths, it is possible to transform the EW and NS component recordings into radial and transverse components and to generate particle motion plots for the identified phases as a confirmation (Figs. 3 to 6 in Tapia et al., submitted).

In order to locate the NR event, once we obtained the back azimuth, we estimate reliable epicentral distances of the event by means of ray-tracing. The time between the P_g and S_g arrivals is (t_s-t_p) = 2.38 ± 0.05 s. We consider the error higher than the sampling
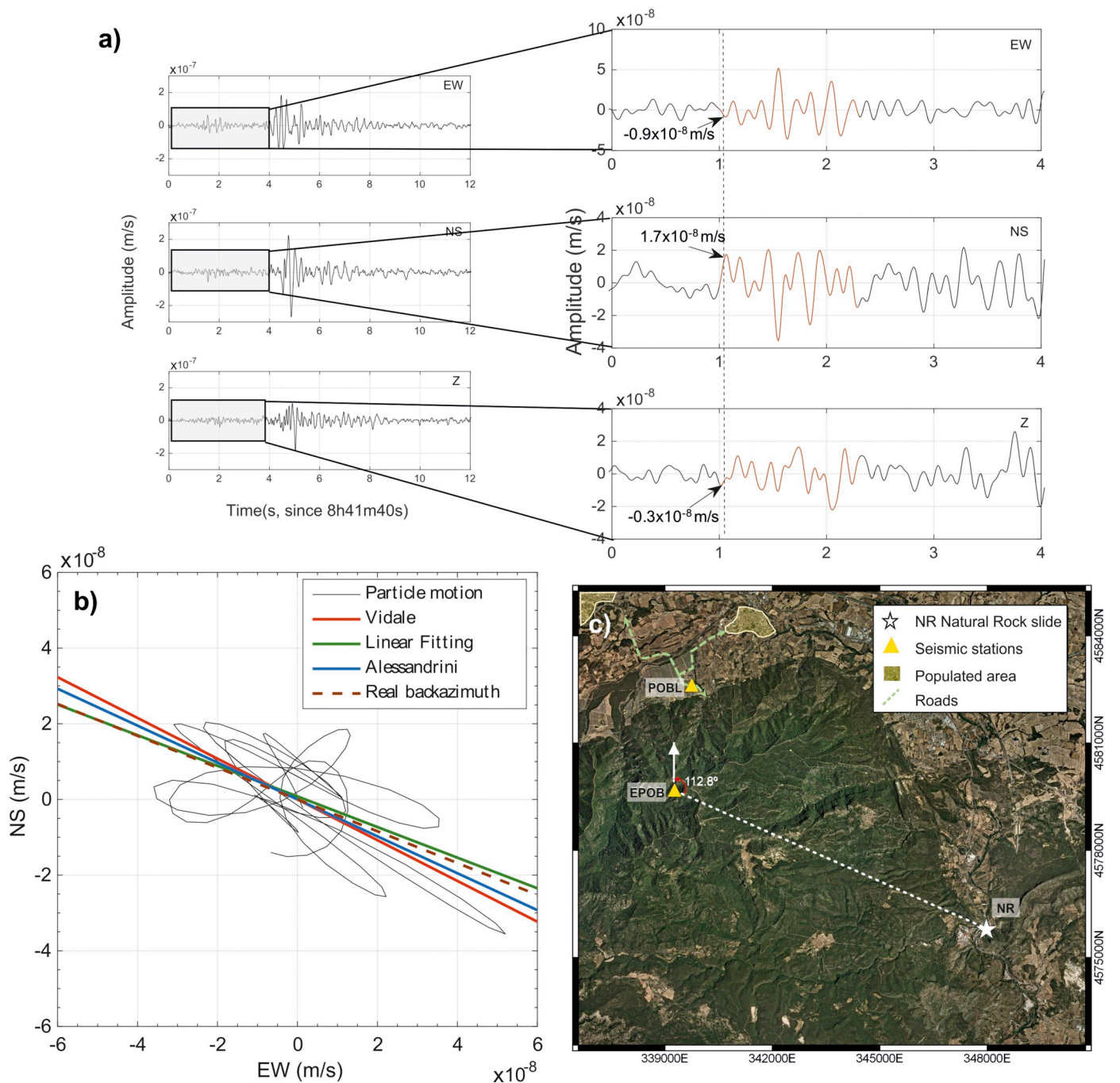
Fig. 6. a) EPOB seismic data 1–12 Hz filtered by a fourth order Butterworth high pass filter (left). At right, zoomed plot where seismic waveforms (indicated in orange) correspond to the time window used to perform the particle motion plot (b). Indicated amplitude values were used to compute the back azimuth following Alessandrini et al. (1994) and Havskov et al. (2012) (blue line in b). b) Particle motion plot together with the real back azimuth (dashed brown line) and back azimuth estimations following Vidale (1986) (red line), basic linear fitting (green line), and Alessandrini et al. (1994) (blue line). c) Seismic stations and NR situation map showing the back azimuth between EPOB station and the NR event. Roads near POBL are set as dashed green arrows and the nearest populated areas as yellow polygons. (For interpretation of the references to colour in this figure legend, the reader is referred to the web version of this article.)

resolution due to the difficulty of manually picking the first arrival because of the low signal-to-noise ratio. To estimate an epicentral distance, the expression for direct waves $d = (t_s-t_p)(V_pV_s)/(V_p-V_s)$ is used, where V_p is the P wave velocity and V_s the S wave velocity. Taking into account an ideal Poisson solid, which is a valid approximation for epicentral distances < 100 km, $V_s = V_p/\sqrt{3}$. Since exact values of P waves velocities for the region are not available a priori, P-wave velocities in crustal sedimentary layers range from 2000 to 4000 m/s, depending upon such factors as degree of compaction, water content and lithologic types (Condie, 1997). Taking into account the lack of

precise knowledge about the properties of the sub-surface materials and thus, considering this wide range of velocities, the estimated mean epicentral distance would be 9750 ± 3250 m, which is consistent with the real distance of 9500 m.

On the other hand, applying the known distance of 9500 m between EPOB and the NR event, it is possible to estimate realistic seismic wave velocities for the region, taking into account the observed direct crustal phases of the S- and P-waves within distances < 100 km (ideal Poisson solid $V_s = V_p/\sqrt{3}$). The result is a P velocity wave of 2922 m/s (around 3000 m/s), and a velocity of S-wave of 1687 m/s. Furthermore, taking
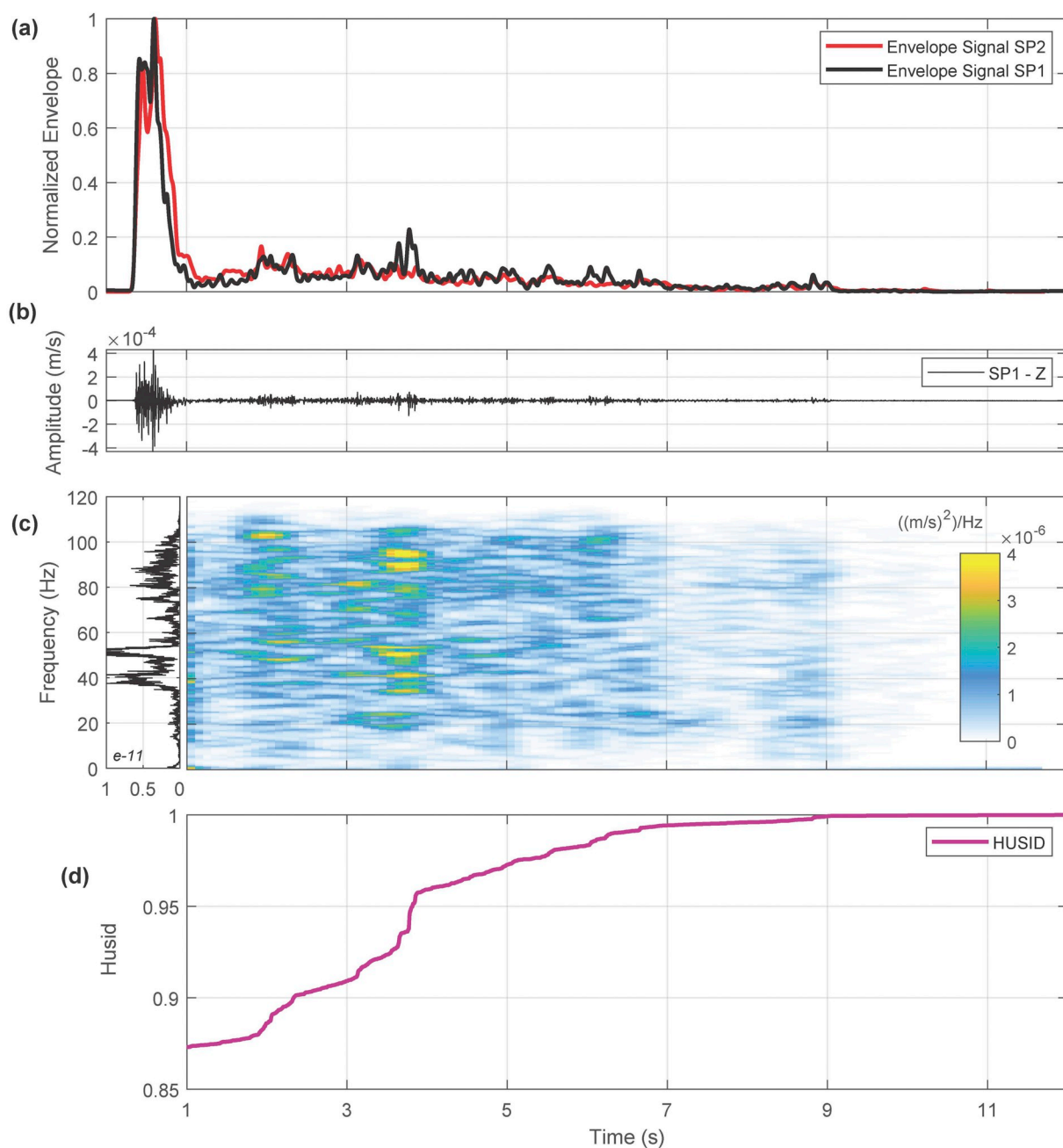
Fig. 7. Analysis of the Sp1 and Sp2 seismic record. Blast (0–1 s) and rockfall (1–12 s) seismic records. (a) Sp1 and Sp2 normalized envelopes; (b) Sp 1 vertical seismic record; (c) Spectrogram and Fourier spectrum amplitude; (d) Husid diagram with the duration of the rockfall (t $_{HUSID}$ = 9.1 s).

into account that Rayleigh wave velocity is approximately $0.9V_s$, and Love wave travels slightly faster than Rayleigh wave, an estimated surface wave velocity for the area is around 1500 m/s, implying that surface waves arrive 0.6–0.7 s after S_g, which matches well with the seismic record (Fig. 5). These deduced seismic velocities in the region will be used in the seismic energy estimations (Section 8).

7. Seismic signal and video correlation for kinematic description of the Main-Blast (MB) event

The proximity of the Sp1 and Sp2 dedicated seismic stations to the MB site (Section 3) and the high sampling rate (250 Hz) of the data, offer a wide range of frequencies providing insights into the characterization of this type of phenomena. The obtained seismic records (Fig. 7) show the typical characteristics of the seismic signals generated by mass movements (Biescas et al., 2003; Suriñach et al., 2005; Vilajosana et al., 2008; Pérez-Guillén et al., 2016). The normalized envelopes of both Sp1 and Sp2 signals show a good correlation between them (Fig. 7a). The difference in amplitudes between Sp1 and Sp2 can be attributed to the difference in the wavefront propagation azimuths and the site effects. After the blast signal, the record shows a spindle shape, mixed with locally prominent amplitudes associated to large block impacts (Fig. 7b). The time-frequency analysis highlights several intervals of greater amplitudes, characterized by maximum energies in two main frequency bands, one between 40 and 60 Hz and the other between 80 and 100 Hz (Fig. 7c). The blast signal lasted 0.5 s and the duration of the rock fall estimated from seismic records was 9.1 s using the normalized Husid diagram (Husid, 1969) and the Trifunac duration criteria (Trifunac and Brady, 1975) (Fig. 7d). Records from the Sp1 station, set on hard rock, were used to estimate energies and rock
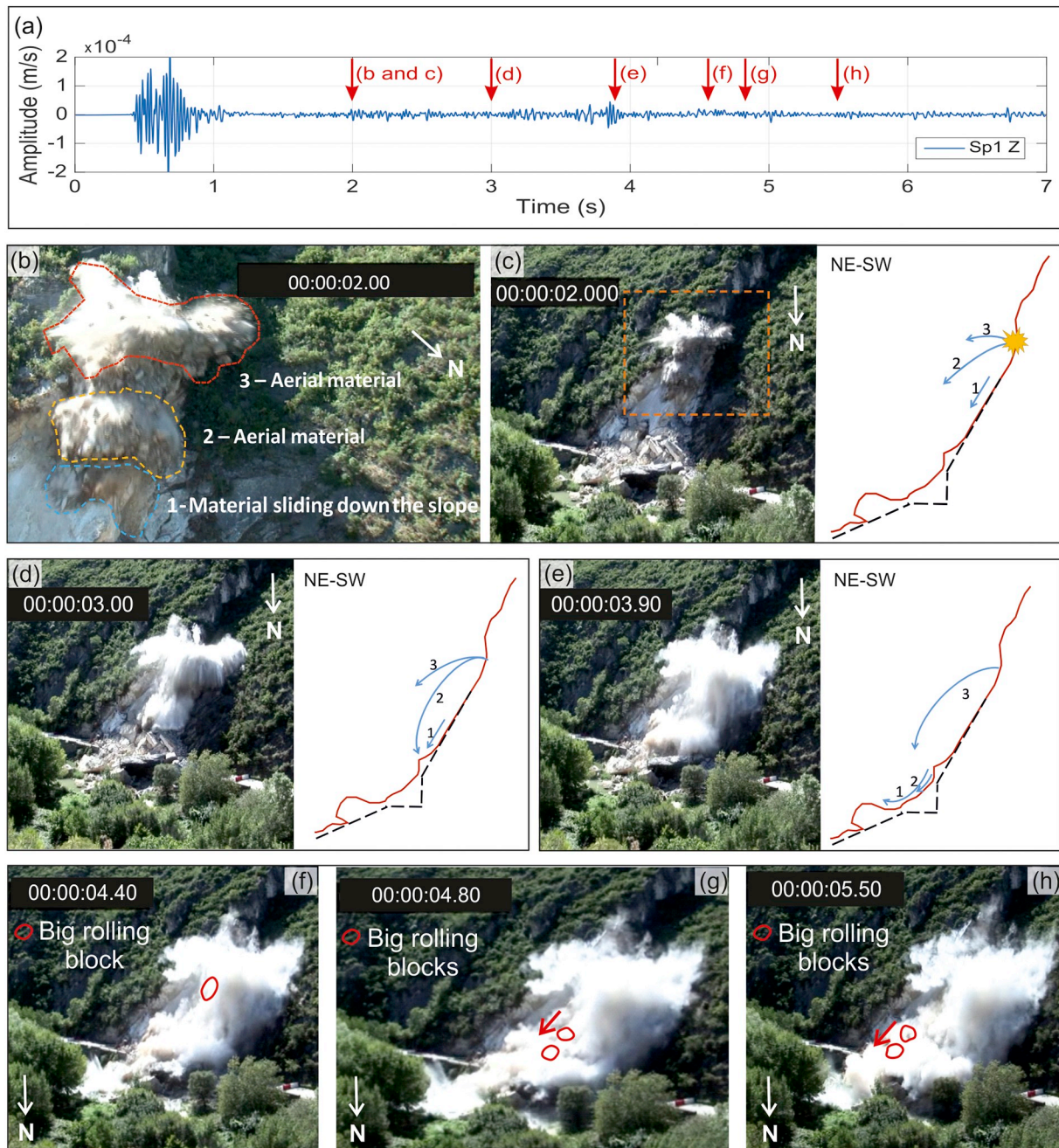
Fig. 8. Identification of different phases of the rock fall in seismic signal and video frames. (a) Seismic record in Sp1 with the blast signal (on the left). (b) 2 s video frame at $t = 2$ s where the group of material sliding down the slope (1) is delimited with a blue dashed line, the group of material suspended into the air closer to the slope (2) with a yellow dashed line and the group of material suspended into the air farther away from the slope (3) with a red dashed line. (c) General view of the video frame at $t = 2$ s and a schematic draw of the three groups of material differentiated in (b). (d) Video frame at $t = 3$ s with a schematic draw showing the moment in which the Groups 1 and 2 reach the road simultaneously. (e) Video frame at $t = 3.9$ s with a schematic draw showing Group-3 reaching the road. (f), (g) and (h) Video frames at $t = 4.4$ s, $t = 4.8$ s and $t = 5.5$ s respectively with the identification of individual blocks rolling down the slope (red circles). (For interpretation of the references to colour in this figure legend, the reader is referred to the web version of this article.)

volumes, since they were less prone to local effects.

The analysis of the seismic signals in the time and frequency domains, together with the video frames, allows the identification of the different phases of the rock fall, providing information about its dynamics. The MB creates three different groups of falling material: 1) materials sliding down the slope (1 in Fig. 8); 2) materials suspended in the air close to the slope, following a parabolic trajectory (2 in Fig. 8); 3) materials farther away from the slope, also with a parabolic trajectory (3 in Fig. 8) as consequence of the blast configuration. These two latter aerial groups consist of a set of rock-blocks of about

0.15×10^{-3} m³ or less. The sliding rock-block (Group-1) included a wider range of sizes.

In the time interval between 1 and 2 s after the blast, the Group-1 started to slide down the slope, while the Groups 2 and 3 continued to be suspended in the air (Fig. 8a, b, and c). During this interval the recorded seismic signal was of low amplitude, which increased gradually as the sliding material approached the seismic stations. Materials from the Group-2 were superimposed on the sliding materials along the slope just before $t = 2$ s, as deduced by the higher seismic amplitudes (Fig. 8a). The video analysis shows that the front of the flowing material

(Groups-1 and 2) reached the road at $t = 3$ s simultaneously (Fig. 8a and d). At this time, the seismic amplitudes were not especially high (Fig. 8a), likely because no large blocks impacted on the road. This suggests that aerial material of Group-2, which was closer to the surface than the Group-3, was gradually depositing material on top of Group-1 along the slope. On the other hand, the material of the Group-3 reached the road as a whole block just before $t = 4$ s (Fig. 8a, and e). The effect of the block impacts is visible in the seismic record with locally higher amplitudes. Around this time, the remaining material of Group-1 seized its sliding on the slope, while a couple of large blocks also rolled down independently, impacting the road in the interval $t = 4.4$ s to $t = 5.6$ s (Fig. 8a, f, g, and h). From t = 5.6 s to t = 10 s a decrease in the seismic amplitudes was observed (Fig. 8a). At a time instant of t = 10 s the recorded amplitudes reached the seismic noise level, which was interpreted as the end of the rock fall. Since the dust cloud remained during at least 10 s following the mass movement, solely from the video recordings it was impossible to deduce the exact time when the triggered rock fall had stopped its motion. For this reason, the end time had to be deduced from the seismic signal.

8. Seismic energy, potential energy, E_s/E_p ratios and volume estimations

This section focuses on the calculation of energies and E_s/E_p ratios for volume estimation of future events. On one hand, the potential energy was calculated through the previous estimation of volumes, whereas seismic energy was estimated from the recorded seismic data. The comparison of both energies results in E_s/E_p ratios and in volumes estimated solely from seismic energy. In turn, seismic energy was estimated using two methodologies: an empirical one with the calculation of seismic magnitudes and a theoretical one based on wave propagation theory.

8.1. Potential energy from previously estimated volumes

The total displaced volume during the natural rock slide (NR) was about $V = 475–506$ m^3, as described above (Section 5 and Table 1), which slid for 15 to 20 m downslope. Assuming that the entire volume impacted the road after a free fall of h = 15 m, and supposing a rock density of $\rho = 2700$ kg/m^3, consistent with the type of rocks at the site, the potential energy would be $E_p = mgh = \rho V g h = 189–201$ MJ. We considered $E_{pNR} = 201$ MJ as an upper limit, because most likely, the fallen volume did not hit the road as a single block and thus, some part of the energy was dissipated by the block friction downslope. We assume that the seismic energy is produced by the largest part of material impacting as a single block onto the road. The remaining volume would hit the road in smaller pieces, generating low seismic energy, which is hard to distinguish in the recorded seismic data. The potential energy associated to the main-blast (MB) event deduced from the volumes estimated from LiDAR and photogrammetry data (Table 1) is $E_{pMB} = 48–54$ MJ.

8.2. Seismic energy of the Natural Rock slide (NR) from estimated magnitudes

Although the two events considered in this study (NR and MB) occurred in the same location, they are characterized by completely different dynamics and seismic characteristics. The NR event is generated mainly by the slide of a single large block, which impacted on the road with a relative low velocity. The MB event, however, involved material of different sizes, which partly moved suspended in the air, partly flowed and partly bounced, and finally impacted along the slope and on the road. The differences in the seismic characteristics include that the NR was recorded around 10 km far and that the signal is dominated by surface waves, whereas the MB event was recorded < 100 m away from the source and its seismic record is dominated by body waves.

Given the clear maximum amplitude of the surface waves generated by the NR event recorded at EPOB and POBL stations, it seems appropriate to estimate the magnitude of this falling block following the same procedures as for a small local earthquake (Bottelin et al., 2014; Lacroix and Helmstetter, 2011). However, this method is mainly empirical, and the main factors related with the nature of the rock slide and the geotechnical characteristics of the ground are not considered. The magnitude of the event was calculated using the fitted local seismic magnitude scale for the EPOB station (Eq. 1) defined by its operator IGN (Spanish National Geographic Institution) (IGN, Instituto Geográfico Nacional, 2017).

$$M_{IGN} = \log(V_{max}/2\pi) + 1.17\log(d) + 0.0012(d) + 0.67 \quad (1)$$

where V_{max} (µm/s) is the maximum amplitude for surface waves and d (km) is the source-receiver distance.

The obtained magnitude was $M_{IGN} = 0.3$ from the EPOB record and $M_{IGN} = 0.8$ from POBL. The aforementioned site effects (Section 6.1) most likely cause this considerable difference in the calculated magnitudes from the two stations. The magnitude was transformed to energy using Kanamori's (1977) seismic energy law expressed in J (log $E_s = 1.5M_{IGN} + 4.8$) for surface wave magnitudes. The resulting energies are $E_s = 0.2$ MJ for EPOB and 1.0 MJ for POBL.

8.3. Seismic energies of NR and MB from theoretical approach

Theoretically, the computation of the seismic energies (Eq. (2)) must take into account the radiated elastic energy at source, E_{source} (J), assuming an isotropic homogeneous medium, for all the frequency content and signal duration, corrected by the attenuation effects as a function of source-receiver distance (r) and frequency, such as geometrical spreading and the anelastic attenuation. The source amplitude, A_0 (m/s), is estimated for surface waves by Eq. (3) and for body waves by Eq. (4)., where the geometrical spreading correction for surface waves is calculated as a cylinder of radius r and height h, where h is one quarter of the wavelength, and for body waves is calculated as a sphere with radius r.

$$E_{source} = \int_{t_1}^{t_2} \frac{1}{2} c\, \rho\, A_o^2\, dt \quad (2)$$

$$A_o^2 = u_{env}^2(t) 2\pi r h e^{\alpha r} \quad (3)$$

$$A_o^2 = u_{env}^2(t) 4\pi r^2 e^{\alpha r} \quad (4)$$

$$u_{env}(t) = \sqrt{u(t)^2 + ht(u(t))^2} \quad (5)$$

where r (m) is the source-receiver distance, ρ (kg/m^3) is the ground density, c (m/s) is the phase velocity of the seismic waves, $u_{env}(t)$ (m/s) is the amplitude of the envelope of the recorded signal (ground velocity) obtained through the Hilbert transformation (ht) using Eq. (5), and $\alpha = 2\pi f/Qc$ is the damping factor that accounts for anelastic attenuation of waves and depends on the signal frequency f (Hz), the phase velocity, and the non-dimensional quality factor Q that is frequency dependent.

In this work, a centroid frequency is computed at each seismic record and it is used as constant for the presented equations, neglecting its frequency dependence.

The seismic energy of the NR event is calculated using EPOB data located at 9500 m distance. The spectral density of the station EPOB is characterized by a narrow, low-frequency content spectrum (Fig. 7 in Tapia et al., submitted) for the three components. The centroid frequencies calculated for each component are Z: 4.4 Hz, NS: 3.6 Hz and EW: 4.3 Hz, with an average value of 4 Hz. The E_s energy estimated for the NR event is computed assuming that the maximum amplitudes are mainly generated by surface waves (Fig. 5) and thus, by using Eqs. (2) and (3). In the region where the seismic stations are located, an experimental Q(f) = 130 has been estimated by Noriega et al. (2015) and Noriega (2016) for very low frequencies (for periods $T = 8–20$ s), which

Table 2

Seismic energies E_s and E_s/E_p ratios using different $Q(f)$, and $\alpha(f)$ values, velocities and densities for the NR and MB events.

Q	ρ (kg/m^3)	NR c = 1500 m/s			MB c = 3000 m/s		
		α(1/m)	E_s (J) for centroid	E_s/E_p (Ep = 201 M J)	α(1/m)	E_s (J) for centroid	E_s/E_p (Ep = 54 M J)
			f = 4 Hz			f = 64 Hz	
15	2700	1.1×10^{-3}	4.4×10^5	2.2×10^{-3}	8.9×10^{-3}	9146	1.7×10^{-4}
25		6.7×10^{-4}	6298	3.1×10^{-5}	5.4×10^{-3}	6995	1.3×10^{-4}
50		3.4×10^{-4}	261	1.3×10^{-6}	2.7×10^{-3}	5721	1.1×10^{-4}
70		2.4×10^{-4}	105	5.2×10^{-7}	1.9×10^{-3}	5293	9.8×10^{-5}
100		1.7×10^{-4}	54	2.7×10^{-7}	1.3×10^{-3}	4993	9.2×10^{-5}
130		1.3×10^{-4}	36	1.8×10^{-7}	1.0×10^{-3}	4843	9.0×10^{-5}
150		1.1×10^{-4}	30	1.5×10^{-7}	9.0×10^{-4}	4779	8.8×10^{-5}
300					4.5×10^{-4}	4564	8.5×10^{-5}
E_s/E_paverage			**3.2×10^{-4}**				**1.1×10^{-4}**

do not exactly match the 4 Hz of centroid frequency in EPOB data, but it is the only available experimental data of the area. Due to the uncertainty of the exact values of Q for the region, we have used values of Q ranged from 15 to 150 to estimate the energy. In this range of values, it is also included the quality factor estimated by Noriega (2016). The velocity of surface waves was estimated to be ~1500 m/s from the wave picking analysis detailed in Section 6.1. We estimate the energy using a standard density of 2700 kg/m^3 in agreement with Boore and Joyner (1997). The E_s estimated using different values of Q and α are shown in Table 2. The seismic energies estimated increase exponentially as a function of 1/Q, showing a very large range of values from 30 J to 4.4×10^5 J, which differs up to four orders of magnitude.

The energy for the MB event was calculated with Sp1 seismic station data at a distance of 75 m, assuming body waves as expressed in Eqs. (2) and (4), using a velocity of 3000 m/s for body waves, deduced in Section 6.2. The station proximity results in a higher frequency content, where the estimated centroid frequencies for each component are Z: 68 Hz, NS: 59 Hz and EW: 66 Hz with an average value of 64 Hz (Fig. 7). We follow the same procedure as in Section 8.1, but, taking into account that Q values increase as a function of frequency (Morozov et al., 2018), and the higher frequency content of the seismic signal, in this case a higher value of Q (Q = 300) was added to the same range of Q used for NR event. E_s values range from 9×10^3 J to 4.6×10^3 J (Table 2).

8.4. E_s/E_p ratios and volume estimations

Using E_{pNR} = 201 MJ and the E_{sNR} values shown in the Table 2, the average E_s/E_p ratio of the NR is 3.2×10^{-4} with a standard deviation of 8.2×10^{-4}, giving a wide range of ratios from 1.5×10^{-7} to 2.2×10^{-3}, due to the high sensitivity of the results at this distance to the uncertainty of the Q value. For a quality factor of Q = 130 (mean value of Noriega et al. (2015) in the region), the E_s/E_p ratio is 1.8×10^{-7}, which is a very low ratio. However, considering the E_s estimated from magnitudes (0.2 MJ for EPOB and 1.0 MJ for POBL), the E_s/E_p ratio increases to 1×10^{-3} for EPOB and 5×10^{-3} for POBL, which are one order of magnitude higher than the mean ratio estimated from the theoretical approach. Since the anelastic attenuation from magnitude approach is $\alpha = 1.2 \times 10^{-3}$ and in the theoretical approach the equivalent value ($\alpha = 1.1 \times 10^{-3}$) is for Q = 15, the results from both methods are consistent, giving an E_s/E_p ratio of 2.2×10^{-3} (Table 2).

For the MB event, considering the E_{pMB} = 54 MJ and the E_{sMB} values obtained from the theoretical approach, the average E_s/E_p ratio of the MB event is 1.1×10^{-4} with a standard deviation of 2.7×10^{-5} (Table 2). The E_s/E_p ratio calculated from the fixed value of Q = 130 (Noriega et al., 2015) is 9.0×10^{-5}, which is close to the mean value. The estimated E_s/E_p ratios for this event are far less disperse than for

the NR event, as we expected due to the short source-receiver distance, resulting in less dependency on the wave propagation phenomena. These two ratios are also in agreement with the results of the literature that report values of E_s/E_p between 10^{-5} and 10^{-3} for granular flows (Levy et al., 2015; Hibert et al., 2011 and Deparis et al., 2008b).

Using the E_s/E_p ratios, we can infer the volumes of future rockfall events in the region from seismic records and estimating seismic energies by using the following expression: $v = E_s / (R\rho gh)$; where v (m^3) is the rockfall volume, E_s (J) is the seismic energy, R is the E_s/E_p ratio, ρ (kg/m^3) is the density, g (m/s^2) is gravity, and h (m) is the height. The calculated MB event volume, estimated considering the E_s/E_p ratios for the NR event estimated from magnitudes (~1×10^{-3}) and from theoretical approach (~3.2×10^{-4}), ranges from 11 to 23 m^3 and from 36 to 72 m^3 respectively, and depending on the Q value used to estimate seismic energy (Table 2). In contrast, more reliable volumes found with remote sensing method range from 121 to 135 m^3). On the other hand, using E_s/E_p ratio estimated for MB event (~1.1×10^{-4}) for recovering volumes of the NR event we obtain values ranging from 1 to 10^4 m^3 depending on the value of Q used to estimate the seismic energy (Table 2). These volumes differ two orders of magnitude from the volume estimated using remote sensing (475–506 m^3).

9. Discussion and conclusions

Photogrammetric, aerial and terrestrial LiDAR surveys yielded consistent volume estimates for both natural and artificially released events, ranging from 475 to 506 m^3 for the natural rock slide (NR) and from 121 to 135 m^3 for the blasting induced rock fall (MB). This study demonstrates the potential of the ground photogrammetry technique for evaluating the volume of displaced material and also, for performing a structural analysis of the cliff, even when limited number of photographs are used (5 photos in this study), limiting the resolution of the 3D model. Moreover, the volume was estimated by fitting planes to the discontinuities derived from the structural analysis, due to the lack of 3D data preceding the event. The estimated volumes from LiDAR and photogrammetry data by subtracting the volume from pre- and post-event point clouds in Polyworks® (InnovMetrics®) or by volume reconstruction in Gocad® (Paradigm®), shows relatively small discrepancies of 6–12% (Table 1). Thus, both LiDAR and photogrammetry data, as well as the two used methodologies (subtracting data and volume reconstruction), provide equivalent results while estimating the volume detached during the events. However, the applicability of the volume reconstruction approach depends on the lithology: in La Riba study area it was possible to use this method, since the rockfall is bounded by planar discontinuities, consisting of limestone bedding and fractures; in other geologic settings this method might not work.

NR event was detected by two seismic stations belonging to permanent seismic monitoring networks and located at ~10 km distance.

These are the only records available for this event, that allowed the retrieval of the occurrence time of the NR. The recorded seismic signal most likely corresponds to the fall of the largest part of the total volume of the NR (Fig. 2), which was certainly accompanied by a fall of smaller rock blocks, whose seismic signal was not possible to distinguish from the background noise.

Usually seismic signals of fragmentary rock falls, rock slides and landslides recorded at shorter distances than for the NR (< 3 km) are longer and their envelopes show a gradual amplitude increase as the rock mass progresses towards the seismic sensor, having a spindle-like shape (Biescas et al., 2003; Suriñach et al., 2005). On the contrary, the characteristics of the recorded seismic signals induced by the NR, co-incide with those described in previous works on individual rock falls and block impacts (Vilajosana et al., 2008; Weichert et al., 1994).

The NR seismic signals are characterized by an impact shape (Fig. 5) with a dominant frequency content up to 15 Hz (Fig. 7 in Tapia et al., submitted), indicating an important role of the attenuation as a function of distance, not only for the amplitude decrease, but also for the decay of the high frequencies. These seismic records are dominated by surface waves that are normally reported in most of similar studies (Rousseau, 1999; Deparis et al., 2008b; Helmstetter and Garambois, 2010; Bottelin et al., 2014). However, in this work it was also possible to identify preceding P- and S-wave body wave phases. Weichert et al. (1994) also describes P_g and S_g waves in seismic detection for a larger rock slide (2×10^6 m³) recorded at distances exceeding 100 km at several stations from the Western Canada Telemetred Network (WCTN).

The P-waves identification allowed us to locate the NR event with a single 3-component seismic station, analysing the polarity of the P-waves and the time duration between P and S waves. Previously, other authors have used more than one station, applying for example, the cross-correlation methods reported in Helmstetter and Garambois (2010); Lacroix and Helmstetter (2011); or Hibert et al. (2014), which cannot be applied in this study. Using three seismic arrays, Lacroix and Helmstetter (2011) estimated the location of rockfalls with location uncertainties of hundreds of metres. The accuracy of our estimated location using a single seismic station is in the order of few kilometres, due to the uncertainties in the seismic wave velocities. With a thorough knowledge of the distribution and characteristics of subsoil materials, a more accurate estimation of the seismic wave velocities could be achieved, which would result in a significant improvement in the ac-curacy of the locations obtained by the single seismic station method.

The seismic signals generated by the MB event are completely dif-ferent from those generated by the NR. In the MB case, data were re-corded at closer distances at temporary stations installed for the ex-periment. In this case, high frequencies are present due to the smaller effect of attenuation over the short distances. The high frequency band allows for qualitative interpretation of the complexity of the rock fall evolution (Bottelin et al., 2014; Hibert et al., 2017). The combined analysis of the seismic and video recordings allows identifying different phases of the induced rock fall. The observed changes in seismic signal amplitudes were detected according to the general evolution of the rock fall and large peaks were associated with isolated impacts. During the MB two differentiated groups of materials were generated due to the configuration of the explosion. The source of the seismic signals was found to be related to the friction and the impacts of the different group of materials on the slope and the road. Both techniques complement each other: without the seismic data it would have been impossible to describe some specific phases of the rock fall, due to the presence of the cloud of dust in the video recordings; and on the contrary, the video helps the identification of particular phases and groups in the seismic record.

The seismic energy and E_s/E_p ratio of the NR event was obtained by following two approaches: a) by estimating a pseudo local magnitude; and b) by applying classical wave propagation theory. The first ap-proach yielded an E_s/E_p ratio of $\sim 10^{-3}$ (Section 8.4). This value is inaccurate due to: a) the magnitude approach is based on a scaling law

derived for regional earthquakes covering the entire Iberian peninsula; and b) the conversion from magnitude to seismic energy is based on an empirical relationship for teleseismic earthquakes (Kanamori, 1977), and not local earthquakes. Employing a similar method, Bottelin et al. (2014) had found 10 times smaller ratios ($\sim 10^{-4}$) for rockfalls with volumes about 2×10^3 m³, using closer seismic records (2.5 km). Deparis et al. (2008b) for larger rockfalls (10^6 m³), observed E_s/E_p ra-tios in the range of 10^{-3} to 10^{-6}. Even though the local magnitude approach has been used in previous studies, possible differences be-tween the source mechanisms and nature of earthquakes and rockfalls should be taken into account. In this study, following the classical wave propagation theory, the obtained E_s/E_p ratios for the NR event, vary greatly between 10^{-7} and 10^{-3}, depending on the used attenuation parameters, showing the high sensitivity to ground characteristics. Constraining the attenuation parameters to the more adequate values for the study region (Q = 130), gives an unrealistic value of $E_s = 36$ J (Table 2) and therefore, a low E_s/E_p ratio of $\sim 10^{-7}$, suggesting that only a very small portion of the released potential energy was converted to seismic energy. The efficiency of conversion of potential energy to seismic energy is much larger using Q = 15, resulting in an E_s/E_p ratio of 2.2×10^{-3} quite similar to the E_s/E_p ratio (1×10^{-3} from EPOB data) estimated by the magnitude approach. This is a quite low Q value for the geological characteristics of the study area, being more char-acteristic of a volcanic region (Koyanagi et al., 1995; Giampiccolo et al., 2004). Nevertheless, previous studies in similar geological contexts used very low values of Q < 20 for surface waves (Vilajosana et al., 2008; Saló et al., 2018).

The seismic energy for the MB event was only estimated using the classical wave propagation theory. The magnitude approach was not used because it does not make sense to characterize a complex signal with a single maximum amplitude. The latter could correspond to a specific moment of the entire evolution of the rock fall, such as the impact of a rock or a percentage of aerial material that hits the road or the slope, as described previously. The mean E_s/E_p ratio for the MB is of the order of 10^{-4}, which is more reliable as the recorded amplitudes are less influenced by the wave propagation phenomena. This value is in accordance with the results of Hibert et al. (2011) for rockfalls in a volcanic area, with the modelling results from Levy et al., 2015 for granular flows and with Deparis et al. (2008b) inventory on alpine rockfalls.

The results show large differences between the NR and MB events. As expected, the E_s/E_p ratio estimate for MB event are significantly more precise than for the NR event, due to the short source-receiver distance and thus, lesser dependence on the wave propagation phe-nomena. If the NR event E_s/E_p ratios were used to infer volumes of the MB event (V~135 m³), it would result in an underestimation of the volumes by one order of magnitude. On the other hand, using the va-lues of the E_s/E_p ratio from the MB event to estimate the volume of the NR event, the inferred volumes would be between 1 and 10^4 m³, which differs up to two orders of magnitude from the volumes obtained by remote sensing data (~506 m³), due to the Q dependency not only in the E_s/E_p ratio but also in the E_s estimation.

These results demonstrates that without the exact knowledge of the attenuation parameters along the path, a reliable value of the E_s/E_p ratio cannot be estimated properly and applied in future events to de-duce the volumes, especially in cases of different source-receiver dis-tances. The volume deduced from remote sensing of the NR event is approximately four times the volume of the MB event. The seismic energy estimated for the NR event, however, is up to two orders of magnitude less than for the MB for Q $\geq$ 50 (Table 2), with the result of a large difference in the values of the estimated E_s/E_p ratios. Although we used the same methodology to estimate the energy of both events, the seismic energies estimated of the NR event are lower, since part of the seismic energy is dissipated at a large source-receiver distance of 10 km. If we estimate the seismic energy of the MB only considering a frequency band of 1–10 Hz (equivalent to the frequency content of NR

event), we obtain that the average seismic energy is only the 0.4% of the total seismic energy (Table 2; MB event). This is critical at a large source-receiver distance because only this frequency band is recorded (Fig. 7 in Tapia et al., submitted). Therefore, the estimated low values of seismic energies of the NR event for $Q \geq 50$ (Table 2) are justified. The methods to infer the volumes of future rockfall events at a given site usually involve the calibration of the rockfall volumes with the estimated E_s/E_p ratios. For a reliable volume calculation, the seismic energy should be estimated at similar source-receiver distances and geology conditions should be taken into account. According to our results, it is advisable that the source-receiver distances be kept as short as possible due to two reasons: 1) to register the high frequencies of the rockfall phenomenon, 2) to decrease the effect of the uncertainties on the geotechnical parameters of the area.

Therefore, in our opinion, in studies involving small volumes ($< 10^3 \, \mathrm{m}^3$) and for medium and long distances ($> 10 \, \mathrm{km}$), it is not possible to obtain a reliable volume from the indirect measurements of the seismic energy. However, this is not the case for short distances ($< 10 \, \mathrm{km}$) where less dispersion occurs and reliable volume can be estimated. The conversion of potential energy E_p to seismic energy E_s is too low, similar to the results obtained by other authors in similar studies cited above.

The design and construction of typical fences for rockfall mitigation involves the knowledge of specific variables such as the event location, their frequency of occurrence and their precise volumes. Successive LiDAR scans or periodic photos taken in a rockfall vulnerable area provide a catalog of rockfall activity, as well as, detailed information about rockfall source zones and pre-failure movements, very valuable for rockfall risk prevention. Our results show the feasibility of using LiDAR and/or photogrammetry techniques for a precise estimation of the volume of a rockfall event. Even though deducing rockfall volumes from a LiDAR system are more accurate, the volumes estimated using photogrammetry give similar results ($< 12\%$ discrepancy), illustrating the usefulness of this cost-effective technique. Inferring rockfall volumes from the seismic analysis is much less precise as the method strongly depends on the E_s/E_p ratios, which have to be deduced from a large number of events detected at similar source-receiver distances. This procedure requires a prior knowledge of the displaced volumes obtained by other techniques (e.g. LiDAR or photogrammetry). Nevertheless, seismic sensors show the advantage of providing continuous data, at a rather low economic cost, that can be used for event location, characterization and further volume estimation. Moreover, in comparison with a LiDAR system and conventional cameras, seismic sensors are able to acquire data at a larger source-receiver distances independently from visibility and weather conditions. Integrating both remote sensing techniques such as LiDAR and/or photogrammetry with seismic data should allow the development of a reliable and automatic rockfall monitoring system.

Acknowledgements

References

Abellán, A., Oppikofer, T., Jaboyedoff, M., Rosser, N., Lim, M., Lato, M., 2014. Terrestrial laser scanning of rock slope instabilities. Earth Surf. Process. Landf. 39, 80–97. https://doi.org/10.1002/esp.3493.

Abellán, A., Derron, M.-H., Jaboyedoff, M., 2016. "Use of 3D Point Clouds in Geohazards" special Sissue: current challenges and Future Trends (Editorial). Remote Sens. 8 (2), 130. https://doi.org/10.3390/rs8020130.

AgiSoft, 2012. AgiSoft PhotoScan User Manual Professional Edition, Version 0.8.5. AgiSoft LLC Publication.

Alessandrini, B., Cattaneo, M., Demartin, M., Gasperini, M., Lanza, V., 1994. A simple P-wave polarization analysis: its application to earthquake location. Ann. Geofis. XXXVII (N 5), 883–897.

Bard, P.Y., Bouchon, M., 1985. The two dimensional response of sediment-filled valleys. Bull. Seismol. Soc. Am. 75 (2), 519–541.

Bard, P.Y., Riepl-Thomas, J., 2000. Wave propagation in complex geological structures and their effects on strong ground motion. In: Kausel, E., Manolis, G. (Eds.), Chapter 2 in Wave Motion in Earthquake Engineering. WIT Press, pp. 37–95.

Battaglia, J., Aki, K., 2003. Location of seismic events and eruptive fissures on the Piton de la Fournaise volcano using seismic amplitudes. J. Geophys. Res. (0148-0227) 108 (B8), 2364. https://doi.org/10.1029/2002JB002193.

Biescas, B., Dufour, F., Furdada, G., Khazaradze, G., Surinach, E., 2003. Frequency content evolution of snow avalanche seismic signals. Surv. Geophys. 24, 447–464. https://doi.org/10.1023/B:GEOP.000.

Boore, D.M., Joyner, W.B., 1997. Site Amplifications for generic rock sites. Bull. Seismol. Soc. Am. 87 (N2), 327–341.

Bottelin, P., Jongmans, D., Daudon, D., Mathy, A., Helmstetter, A., et al., 2014. Seismic and mechanical studies of the artificially triggered rockfall at Mount Néron (French Alps, December 2011). Nat. Hazards Earth Syst. Sci. 14, 3175–3193. https://doi.org/10.5194/nhess-14-3175-2014.

Burtin, A., Hovius, N., McArdell, B.W., Turowski, J.M., Vergne, J., 2014. Seismic constraints on dynamic links be- tween geomorphic processes and routing of sediment in a steep mountain catchment. Earth Surf. Dyn. 2, 21–33. https://doi.org/10.5194/esurf-2-21-2014.

Chen, Y., Mendioni, G., 1992. Object modelling by registration of multiple range images. Image Vis. Comput. 10, 145–155. https://doi.org/10.1016/0262-8856(92)90066-C.

Condie, C.K., 1997. Plate Tectonics and Crustal Evolution, 4th edition. Butterworth-Heinemann9780750633864https://doi.org/10.1016/B978-075063386-4/50002-1.

Dammeier, F., Moore, J.R., Haslinger, F., Loew, S., 2011. Characterization of alpine rockslides using statistical analysis of seismic signals. J. Geophys. Res. 116, F04024. https://doi.org/10.1029/2011JF002037.

Deparis, J., Jongmans, D., Cotton, F., Baillet, L., Thouvenot, F., Hantz, D., 2007. Analysis of rock-fall seismograms in the western alps. vol. 98. Bulletin of Seismological Society of America, pp. 1781–1796. https://doi.org/10.1785/0120070082.

Deparis, J., Fricout, B., Jongmans, D., Villemin, T., Effendiantz, L., Mathy, A., 2008a. Combined use of geophysical methods and remote techniques for characterizing the fracture network of a potential unstable cliff site (the "Roche du Mid", Vercors massif, France). J. Geophys. Eng. 1–17. IOP Publishing. https://hal-insu.archives-ouvertes.fr/insu-00277855.

Deparis, J., Jongmans, D., Cotton, F., Baillet, L., Thouvenot, F., Hanz, D., 2008b. Analysis of Rock-fall and Rock-fall Avalanche Seismograms in the French Alps. Bulletin of the Seismological Society of America. Seismol. Soc. Am. 98 (4), 1781–1796. https://doi.org/10.1785/0120070082.

Dietze, M., Mohadjer, S., Turowski, J.M., Ehlers, T.A., Hovius, N., 2017. Seismic monitoring of small alpine rockfalls - validity, precision and limitations. Earth Surf. Dyn. 5, 653–668. https://doi.org/10.5194/esurf-5-653-2017.

Farin, M., Mangeney, A., Toussaint, R., de Rosny, J., Shapiro, N., Dewez, Th., Hibert, C., Mathon, C., Sedan, O., Berger, F., 2015. Characterization of rockfalls from seismic signal: Insights from laboratory experiments. J. Geophys. Res. 120, 7102–7137. https://doi.org/10.1002/2015JB012331.

García-Sellés, D., Falivene, O., Arbués, P., Gratacós, O., Tavani, S., Muñoz, J.A., 2011. Supervised identification and reconstruction of near-planar geological surfaces from terrestrial laser scanning. Comput. Geosci. 37, 1584–1594. https://doi.org/10.1016/j.cageo.2011.03.007.

Giampiccolo, E., Gresta, S., Rasconà, F., 2004. Intrinsic and scattering attenuation from observed seismic codas in southeastern Sicily (Italy). Phys. Earth Planet. Inter. 145, 55–66.

Girardeau-Montaut, D., Roux, M., Marc, R., Thibault, G., 2005. Change detection on points cloud data acquired with a ground laser scanner. Int. Arch. Photogramm. Remote. Sens. Spat. Inf. Sci. 36 (3), 30–35.

Havskov, J., Bormann, P., Schweitzer, J., 2012. Seismic source location. In: Bormann, P. (Ed.), New Manual of Seismological Observatory Practice 2 (NMSOP-2). Deutsches GeoForschungsZentrum GFZ, Potsdam, pp. 1–36. https://doi.org/10.2312/GFZ.NMSOP-2_IS_11.1.

Helmstetter, A., Garambois, S., 2010. Seismic monitoring of Séchilienne rockslide (French Alps): Analysis of seismic signals and their correlation with rainfalls. J. Geophys. Res. 115, F03016. https://doi.org/10.1029/2009JF001532.

Herring, T., King, R.W., Floyd, M.A., McClusky, S., 2015. Introduction to GAMIT/GLOBK, Release 10.6. Massachusetts Institute of Technology, Cambridge, MA, USA Retrieved from. http://www-gpsg.mit.edu/~simon/gtgk/Intro_GG.pdf.

Hibert, C., Mangeney, A., Grandjean, G., Shapiro, N.M., 2011. Slope instabilities in Dolomieu crater, Réunion Island: from seismic signals to rockfall characteristics. J. Geophys. Res. 116, F04032. https://doi.org/10.1029/2011JF002038.

Hibert, C., Mangeney, A., Grandjean, G., Ballard, C., Rivet, D., Shapiro, N.M., Starlano, C., Maggi, A., Bolssier, P., Ferrazzini, V., Crawford, W., 2014. Automated identification,

location, and volume estimation of rockfalls at Piton de la Fournaise volcano. J. Geophys. Res. Earth Surf. 119, 1082–1105. https://doi.org/10.1002/2013JF002970.

Hibert, C., Malet, J.P., Bourrier, F., Provost, F., Berger, F., Bornemann, P., Tardif, P., Mermin, E., 2017. Single-block rockfall dynamics inferred from seismic signal analysis. Earth Surf. Dyn. 5, 283–292. https://doi.org/10.5194/esurf-5-283-2017.

Hungr, O., Leroueil, S., Picarelli, L., 2014. The Varnes classification of landslide types, an update. Landslides 11, 167–194. https://doi.org/10.1007/s10346-013-0436-y.

Husid, R.L., 1969. Análisis de terremotos: Análisis General, Revista del IDIEM. 8. pp. 21–42 (Santiago, Chile).

ICGC-IEC, Institut Cartogràfic i Geològic de Catalunya-Institut d'Estudis Catalans, 1996. Catalan seismic network. International federation of digital seismograph networks. Other/Seismic Network. https://doi.org/10.7914/SN/CA. (Last Accessed; November 2017).

ICGC-LiDAR data, 2017. Institut Cartogràfic I Geològic de Catalunya. http://www.icgc.cat/en/Public-Administration-and-Enterprises/Downloads/Elevations/Lidar-data (last accessed; December 2017).

IGN, Instituto Geográfico Nacional, 2017. Descripción del tipo de Magnitud. Instituto Geográfico Nacional. http://www.ign.es/web/resources/docs/IGNCnig/SIS-Tipo-Magnitud.pdf (last accessed; November 2017).

Jaboyedoff, M., Oppikofer, T., Abellán, A., Derron, M.H., Loye, A., Metzger, R., Pedrazzini, A., 2012. Use of LIDAR in landslide investigations: a review. Nat. Hazards 61 (1), 5–28. https://doi.org/10.1007/s11069-010-9634-2.

Jurkevics, A., 1988. Polarization analysis of three-component array data. Bull. Seismol. Soc. Am., vol. 785, 1725–1743.

Kanamori, H., 1977. The energy release in great earthquakes. J. Geophys. Res. 82, 2981–2987.

Koyanagi, S., Aki, K., Biswas, N., Mayeda, 1995. Inferred attenuation from site effect-corrected T phases recorded on the island of Hawaii. PAGEOPH 144 (1). https://doi.org/10.1007/BF00876471.

Lacroix, P., Helmstetter, A., 2011. Location of Seismic Signals Associated with Microearthquakes and Rockfalls on the Séchilienne Landslide, French Alps. Bull. Seismol. Soc. Am. 101 (1), 341–353. https://doi.org/10.1785/0120100110.

Lague, D., Brodu, N., Leroux, J., 2013. Accurate 3D comparison of complex topography with terrestrial laser scanner: Application to the Rangitikei canyon (N-Z). ISPRS J. Photogramm. Remote Sens. 82, 10–26. https://doi.org/10.1016/j.isprsjprs.2013.04.009.

Levy, C., Mangeney, A., Bonilla, F., Hibert, C., Calder, E.S., Smith, P.J., 2015. Friction weakening in granular flows deduced from seismic records at the Soufrière Hills Volcano, Montserrat. J. Geophys. Res. 120, 7536–7557. https://doi.org/10.1002/2015JB012151.

Maufroy, E., Chaljub, E., Hollender, F., Bard, P.Y., Kristek, J., Moczo, P., De Martin, F., Theodoulidis, N., Manakou, M., Guyonnet-Benaize, C., Hollard, N., Pitilakis, K., 2016. 3D numerical simulation and ground motion prediction: verification, validation and beyond lessons from the E2VP project. Soil Dyn. Earthq. Eng. 91, 53–71. https://doi.org/10.1016/j.soildyn.2016.09.047.

Mavrouli, O., Corominas, J., 2017. Comparing rockfall scar volumes and kinematically detachable rock masses. Eng. Geol. 219, 64–73. https://doi.org/10.1016/j.enggeo.2016.08.013.

Moore, J.R., Gischig, V., Burjanek, J., Loew, S., Fih, D., 2011. Site effects in unstable rock slopes: dynamic behaviour of the Randa instability (Switzerland). Bull. Seismol. Soc. Am. 101. https://doi.org/10.1785/0120110127.

Moore, J.R., Pankow, K.L., Ford, S.R., Koper, K.D., Hale, J.M., Aaron, J., Larsen, C.F., 2017. Dynamics of the Bingham Canyon rock avalanches (Utah, USA) resolved from topographic, seismic, and infrasound data. J. Geophys. Res. 122, 615–640. https://doi.org/10.1785/012003001. Earth Surface.

Morozov, I.B., Jhajhria, A., Deng, W., 2018. On Strong Positive Frequency Dependencies of Quality Factors in Local-Earthquake Seismic Studies (Article). Pure Appl. Geophys. 2018 (1420-9136) 175 (N.8), 2595–2607. https://doi.org/10.1007/s00024-018-1826-9.

Noriega, R., 2016. Seismic Attenuation Analysis Using Lg Waves and Ambient Noise Recordings: application to the Iberian Peninsula and Morocco. Ph Thesis Universitat de Barcelona. https://www.tdx.cat/bitstream/handle/10803/400704/RNS_PhD_THESIS.pdf?sequence=1.

Noriega, R., Ugalde, A., Villaseñor, A., Harnafi, M., 2015. Frequency-dependent Lg-wave attenuation in northern Morocco. Tectonophysics 663, 250–260. https://doi.org/10.1016/j.tecto.2015.08.010.

Pérez-Guillén, C., Sovilla, B., Suriñach, E., Tapia, M., Köhler, A., 2016. Deducing avalanche size and flow regimes from seismic measurements. Cold Reg. Sci. Technol. 121, 25–41. https://doi.org/10.1016/j.coldregions.2015.10.004.

Rousseau, N., 1999. Study of Seismic Signal Associated with Rockfalls at 2 Sites on the Réunion Island (Indian Ocean): Mahavel Cascade and Soufrière Cavity. PhD Thesis at the Institut de Physique du Globe de Paris, Paris, France, pp. 134.

Royán, M.J., Abellán, A., Jaboyedoff, N., Vilaplana, J.M., Calvet, J., 2014. Spatio-temporal analysis of rockfall pre-failure deformation using Terrestrial LiDAR. Landslides 11, 697–709. https://doi.org/10.1007/s10346-013-0442-0.

Saló, L., Corominas, J., Lantada, N., Matas, G., Prades, A., Ruíz-Carulla, R., 2018. Seismic energy analysis as generated by impact and fragmentation of single-block experimental rockfalls. J. Geophys. Res. 123, 1450–1478. https://doi.org/10.1029/2017JF004374.

Spillmann, T., Maurer, H., Green, A.G., Heincke, B., Willenberg, H., Husen, S., 2007. Microseismic investigation of an unstable mountain slope in the Swiss Alps. J. Geophys. Res. 112 (B07301), 25. https://doi.org/10.1029/2006JB004723.

Suriñach, E., Vilajosana, I., Khazaradze, G., Biescas, B., Furdada, G., Vilaplana, J.M., 2005. Seismic detection and characterization of landslides and other mass movements. Nat. Hazards Earth Syst. Sci. 5, 791–798. https://doi.org/10.5194/nhess-5-791-2005.

Suriñach, E., Tapia, M., Roig, P., Blach, X., 2018. On the effect of the Ground Seismic Characteristics in the Estimation of Mass Movements Based on Seismic Observation. Geophysical Research Abstracts. 20 EGU2018–8479, 2018. EGU General Assembly 2018. https://www.researchgate.net/publication/331284120_On_the_effect_of_the_ground_seismic_characteristics_in_the_estimation_of_mass_movements_based_on_seismic_observation.

Tannant, D.D., Giordan, D., Morgenroth, J., 2017. Characterization and analysis of a translational rockslide on a stepped-planar slip surface. Eng. Geol. 220, 144–151. https://doi.org/10.1016/j.enggeo.2017.02.004.

Tapia, M., Guinau, M., Roig, P., Perez-Guillen, C., Suriñach, E., Khazaradze, G., Torné, M., Royán, M.J., Echeverria, A. Submitted. Seismic data of a rockslide: evaluation of noise levels, site effects, frequency content and identification of seismic phases. Data in Brief. ISSN: 2352-3409.

Thompson, E.M., Baise, L.G., Kayen, R.E., Guzina, B.B., 2009. Impediments to predicting site response: Seismic property estimation and modelling simplifications. Bull. Seismol. Soc. Am. 99 (5), 2927–2949. https://doi.org/10.1785/0120080224.

Trifunac, M.D., Brady, A.G., 1975. A study on the duration of strong earthquake ground motion. Bull. Seismol. Soc. Am. 65 (3), 581–626.

Tripolitsiotis, A., Daskalakis, A., Mertikas, S., Hristopulos, D., Agioutantis, Z., Partsinevelos, P., 2015. Detection of small–scale rockfall incidents using their seismic signature. In: Third International Conference on Remote Sensing and Geoinformation of the Environment. 953519 International Society for Optics and Photonics, (RSCy2015). https://doi.org/10.1117/12.2192591.

Vidale, J.E., 1986. Complex polarization analysis of particle motion. Bull. Seismol. Soc. Am. 76 (5), 1393–1405.

Vilajosana, I., Suriñach, E., Abellán, A., Khazaradze, G., García, D., Llosa, J., 2008. Rockfall induced seismic signals: case study in Montserrat, Catalonia. Nat. Hazards Earth Syst. Sci. 8, 805–812. https://doi.org/10.5194/nhess-8-805-2008.

Weichert, D.W., Horner, R.B., Evans, S.G., 1994. Seismic Signatures of Landslides: the 1990 Brenda Mine Collapse and the 1965 Hope Rockslides. Bull. Seismol. Soc. Am. 84 (5), 1523–1532.

Williams, J.G., Rosser, N.J., Hardy, R.J., Brain, M.J., Afana, A.A., 2018. Optimising 4-D surface change detection: an approach for capturing rockfall magnitude-frequency. Earth Surf. Dyn. 6, 101–119. https://doi.org/10.5194/esurf-6-101-2018.

Yamada, M., Matsushi, Y., Chigira, M., Mori, J., 2012. Seismic recordings of landslides caused by Typhoon Talas (2011), Japan. Geophys. Res. Lett. 39, L13301. https://doi.org/10.1029/2012GL052174.

Zimmer, V.L., Sitar, N., 2015. Detection and location of rock falls using seismic and infrasound sensors. Eng. Geol. 193, 49–60. https://doi.org/10.1016/j.enggeo.2015.04.007.